



Tuberculosis and HIV responses threatened by nCOVID-19: A situation prompting an *in silico* investigation of reported MbtA inhibitors for combined inhibition of SARS-CoV-2 and HIV-TB co-infection

Gourav Rakshit¹ · Venkatesan Jayaprakash¹

Received: 5 April 2022 / Accepted: 2 July 2022 / Published online: 12 July 2022

© The Author(s), under exclusive licence to Springer Science+Business Media, LLC, part of Springer Nature 2022

Abstract

The menace of infectious diseases has constantly been a reason of concern for humankind since time immemorial. As evident by the name, infectious diseases can infect a huge population within a short period, leading to an eruption of pandemics and epidemics. The present human era is fortunate enough to have a wide array of readily available drugs that help cure and prevent various diseases. Moreover, the scientific community has always responded to the needs of society through its drug discovery and development programs. The co-existence of multiple diseases calls forth the scientific community to design and develop drugs that could have a broad spectrum of activity. In this perspective, our goal was to investigate the potential of reported MbtA inhibitors (antitubercular molecules) in inhibiting HIV-1 RT and nCovid-19-RdRp and eventually leading to the identification of a multi-targeted ligand (triple co-infection inhibitor). In this study, the primary success was attained by capitalizing on the structure-based virtual screening drug discovery approach. Results were quite promising. Molecular docking results showed that GV17 interacted strongly with the active site residues of both the target proteins (HIV-1 RT and nCOVID-19-RdRp). Moreover, the docking score of GV17 was more than that of the internal ligands of both the target proteins, which indicates a firm binding. Molecular dynamics further validated these results as identical amino acid residues were observed in the protein's docked pose with the ligand. The detailed atomic interactions of ligand GV17 with the protein residues have been discussed. Overall, the protein–ligand complexes remained stable throughout the simulation, and the system's backbone fluctuations were modest. MM-GBSA analysis revealed free binding energy of -72.30 ± 7.85 kcal/mol and -65.40 ± 7.25 kcal/mol for 1RT2 and 7BV2, respectively. The more negative binding energy indicates a stronger affinity of GV17 with both the receptors. GV17 also gave satisfactory predictive *in silico* ADMET results. Overall, this computational study identified GV17 as a potential HIT molecule and findings can open up a new avenue to explore and develop inhibitors against nCOVID-19-HIV-TB triple-infections.

Keywords Triple co-infection · nCOVID-19-HIV-TB · MbtA inhibitors · Molecular docking · Molecular dynamics · Predictive ADMET

Introduction

The current human population has been unfortunate enough to witness many deadly infectious diseases of diverse origins. Since ancient times, human civilizations have seen conditions like smallpox [1], plague [2], malaria [3],

influenza [4], tuberculosis [5], HIV [6], cholera [7], rabies [8], pneumonia [9], Ebola [10], variant Creutzfeldt–Jakob disease [11], Marburg virus [12], Middle East respiratory syndrome (MERS) [13], dengue [14], yellow fever [15], hantaviruses [16], anthrax [17], MRSA “superbug” [18], pertussis [19], tetanus [20], meningitis [21], syphilis [22], SARS [23], leprosy [24], measles [25], and Zika [26]. Any onset of these infectious diseases has the potential to disrupt the health care systems mainly due to overburdening in the number of cases and limiting usual general activities, and also hampering the individual's health. The current population was in the war course of dealing with various infectious diseases, when nCOVID-19 (also known as SARS-CoV-2)

✉ Venkatesan Jayaprakash
venkatesanj@bitmesra.ac.in

Gourav Rakshit
gouravr16@gmail.com

¹ Department of Pharmaceutical Sciences & Technology, Birla Institute of Technology, Mesra, Ranchi 835215, Jharkhand, India

came into the battlefield to give a tough fight to humanity [27]. With cases rising daily since its emergence in Wuhan, Hubei Province of China, in December 2019, it was declared a pandemic by the World Health Organization (WHO). Currently, there are no antiviral drugs with proven efficacy against SARS-CoV-2, although several vaccines are now available. Despite vaccinations (11,864,214,773 doses [as of June 15, 2022]) being administered, there have been globally 533,816,957 confirmed cases of SARS-CoV-2, and the total number of deaths reported is 6,309,633 [28]. Immune-compromised individuals and patients with multimorbidity such as those with human immunodeficiency virus (HIV) or tuberculosis (TB) seem more vulnerable to nCOVID-19 infection-causing devastating inflammatory tissue damage leading to ICU (ventilators) admission and death in most cases. Moreover, the emergence of various other strains (Delta, Omicron etc.) and various opportunistic infections also adds to the current viral load. The underlying fact seems that nCOVID-19's pathogenicity may be amplified in HIV-positive/TB persons with weakened immune systems, as TB is the most common opportunistic infection among HIV patients [29]. Here comes this concept of co-infection which refers to the association of two or more clinical conditions or the co-existence of multiple chronic/acute conditions in a single individual at a rate higher than expected by chance. These related diseases may have distinct etiopathogenesis (if the etiology is unknown, with specific pathophysiology of the organ or system) and are present in the same person in a defined period. They usually require co-administration of various treatment regimens involving several medications simultaneously.

As per the WHO's global tuberculosis report 2021, the incidence and mortality of TB patients has worsened since the onset of nCOVID-19 due to a rise in co-infection cases [30]. The primary site of infection in both pathogenic conditions is the respiratory tract system, particularly the lungs. The situation became grimmer with the onset of reports from HIV-infected patients as people with HIV are more susceptible to coronavirus infection because of their immunological state, which renders them tuberculosis-prone also.

As per the literature, there have been several reported cases of triple co-infections since the emergence of nCOVID-19 of which several instances had life-threatening consequences, including respiratory failure, shock, and organ failure. Among them, few have been discussed here: (i) Tolossa et al. [31] reported a case of triple co-infection of nCOVID-19, HIV, and TB in which the patient recovered after getting in-time medical attention. (ii) Ortiz-Martínez et al. [32] reported a fatal death case of a female patient with triple co-infection (HIV/TB/SARS-CoV-2). The nCOVID-19 infection puts TB and HIV responses in jeopardy. (iii) Rivas et al. [33] presented a case report of two patients who recovered from triple infection with TB, HIV, and SARS-CoV-2 by administration

of antitubercular and antiretroviral therapies simultaneously. (iv) Farias et al. [34] reported two cases of co-infection. Both subjects had pulmonary TB and HIV and developed SARS-CoV-2 infection during the 2020 pandemic. As per the report published by Sarkar et al. [35], patients with TB and HIV have an increased mortality risk during a co-infection with SARS-CoV-2. Zhu et al. [36] described the recovery of an HIV-infected patient with coronavirus-related pneumonia. Kumar et al. [37] reported a case of SARS-CoV-2 and TB co-infection in which the patient lost his life due to worsening respiratory parameters. These incidences justify the existence of co-infections that require urgent attention.

To add on, nCOVID-19 is already influencing TB and HIV control strategies. Globally in 2020, apart from 1.3 million deaths due to TB, there were additional 214,000 deaths among HIV-positive patients who were TB infected. HIV, TB, and HIV-TB mortality have been more severely impacted by the nCOVID-19 pandemic with a first 5.6% year-on-year increase in the deaths [30]. This has led to reversal in the years of global progress. The underlying facts seem to be the depletion of CD4 T cells in HIV and latent TB infection which destroys the integrity and design of TB granulomas in the lungs, allowing active TB to develop [38]. TB, too, creates a habitat that aids HIV multiplication through various mechanisms. In fact, after SARS-CoV-2 or TB, permanent improvements in lung architecture play a vital role in both SARS-CoV-2 and TB pathogenesis. Because triple pandemics are linked in the immune-pathological phase, co-infection with SARS-CoV-2, HIV, and TB might have negative implications in all SARS, HIV, and TB phases, forming a fatal loop [39]. Finally, due to the simultaneous use of antitubercular medications, antiviral therapies, and various nCOVID-19 therapy alternatives in a patient, there is a risk of drug–drug interactions and additive hepatotoxicity, which may further deteriorate the health condition of the patient. Hence in this pandemic era, one of the primary and chronic global health issues of the twenty-first century seems to be the threat due to nCOVID-19 in patients with TB or TB-HIV co-infection. These challenges demand for the identification of a single moiety with a broad spectrum of activity.

In an attempt to find a multi-targeted ligand/single moiety here, we hypothesized to repurpose MbtA inhibitors (antimycobacterial agents) which are nucleotide analogues having proven affinity towards MbtA [40, 73]. These compounds being nucleotides gained our interest as we were in search for a chemical scaffold to target an appropriate vital protein in pathogens causing TB, HIV/AIDS, and nCOVID-19 infections/co-infections. Hence, we selected targets (HIV-1 reverse transcriptase (RT) and RNA-dependent RNA polymerase (RdRp) from SARS-CoV-2) for which the substrates were invariably nucleotides. Therefore, an appropriately

designed nucleotide analogue (MbtA inhibitor) could have affinity towards all the three target proteins. We computationally validated this concept by performing molecular docking, molecular dynamics, post-MMGBSA analysis, and predictive *in silico* ADMET analysis. This study may rekindle the interest on the design and development of MbtA inhibitor and also pave a path for future multi-targeted ligand discovery against HIV-TB-nCOVID-19 co-infection. Avenues are open for the scientific community and researchers to explore this concept further.

Materials and methods

Molecular docking

Hardware and software employed

All simulation studies were performed on DELL workstation running Ubuntu 20.04.3 LTS (64-bit as OS, Intel® Core™ i7-11,800 CPU@2.30 GHz processor, 16 GB RAM, 4 GB GPU). AutoDock 4.2.6 and MGLTools 1.5.6 were employed for molecular docking simulations. Molecular dynamics simulations (MDSs) were carried out using the Desmond module of Schrodinger Suite developed by the D. E. Shaw Research group (academic license) [41]. All ligand structures were prepared using ChemOffice Suite 2019 by PerkinElmer Informatics. The 2D/3D protein–ligand interactions were visualized using BIOVIA Discovery Studio Visualizer (Molecular Graphics Environment; Dassault Systemes) [42]. All co-crystallized protein structures were obtained from the Protein Data Bank (PDB) [43] or AlphaFold Protein Structure Database [44].

Protein structure preparation

Two proteins were employed in this study: HIV-1 reverse transcriptase (PDB ID: 1RT2) [45] and RdRp from SARS-CoV-2 (PDB ID:7BV2) [46]. The X-ray crystal structures were downloaded from the PDB. The proteins were in complex with an inhibitor (internal ligand). The internal ligand was separated from the respective co-crystallized protein structures by using UCSF Chimera 1.16 [47]. The protein structure was then opened in the AutoDock 4.2.6 program [48]. The protein preparation steps involved (a) removal of water molecules, (b) addition of polar hydrogen, (c) designating AD4 atom type, and (d) addition of Gasteiger charges to the protein system. Also, selected flips to residues were applied and all-atom contacts were analyzed. The final protein structures were saved in *.pdbqt* format for further simulation studies. The energy minimization of these protein structures was performed using the YASARA server (<http://www.yasara.org/minimizationserver.htm>) [49].

Ligand preparation

The reported MbtA inhibitors have been used here as ligands for screening against HIV-1 RT (PDB ID: 1RT2) and RdRp from SARS-CoV-2 (PDB ID: 7BV2). They can be broadly classified into four categories concerning their structural scaffolds: (a) by linker modification (GV01–GV09), (b) by aromatic group modification (GV10–GV19), (c) sugar moiety modification (GV20–GV25), and (d) base modification (GV26–GV38) [40]. These ligand molecules are mentioned in Table 1 with their details. The ligand preparation steps involved (i) sketching individual structures in ChemDraw 19.1, (ii) energy minimization using the MM₂ module present in Chem3D 19.1, and (iii) saving the final energy-minimized structure in *.pdb* format for protein–ligand docking.

Validation of docking procedure

Given the wide variety of docking and scoring functions available and the heterogeneity in their performance with different targets, it is evident that performing a docking validation study before commencing any virtual screening experiment/docking is essential [50]. The redocking was done to examine the docking procedure and efficiencies. The docking procedure was validated using method; viz., (i) the TNK inhibitor (internal ligand) from the HIV-1 RT and F58 from the RdRp of SARS-CoV-2 was extracted using UCSF Chimera 1.16 and redocked into the active site using AutoDock 4.2.6. Similar grid parameters were adopted. This exercise ensures the inhibitor's exact binding in the active site. The deviation must be less compared to that of the co-crystallized complex available in the Protein Data Bank. The redocked complex was then superimposed onto the reference co-crystallized complex using AutoDock 4.2.6, and the root mean square deviation (RMSD) was calculated.

Theoretical concept involved The AutoDock 4.2.6 scoring function is evaluated by using the experimentally observed protein–ligand complex as a positive control and calculating the RMSD of the other docked ligands with respect to this bound ligand [51]. Through the following equation, the RMSD compared the average distance between atoms of two ligands:

$$\text{RMSD}(a, b) = \sqrt{\frac{1}{n} \sum_{i=1}^n (a_{ix} - b_{ix})^2 + (a_{iy} - b_{iy})^2 + (a_{iz} - b_{iz})^2},$$

where $a \sim i \sim$ refers to the atoms of molecule 1 and $b \sim i \sim$ to the atoms of molecule 2, respectively; the subscripts x , y , and z denote the x – y – z coordinates for every atom.

Table 1 Tabular representation of 38 reported molecules (MbtA inhibitors) employed as ligands in the current study with their code, structure, and details

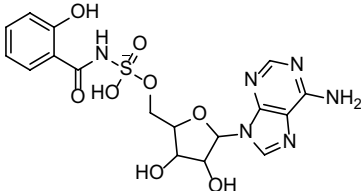
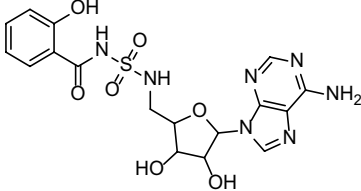
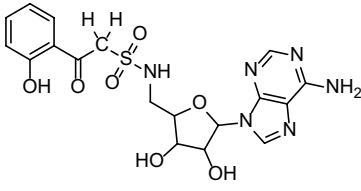
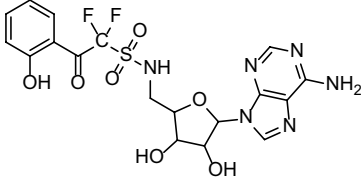
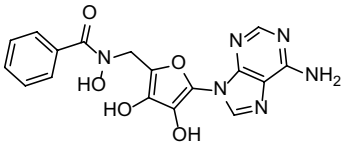
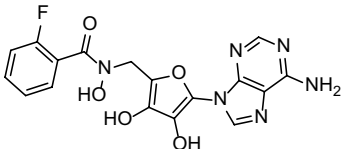
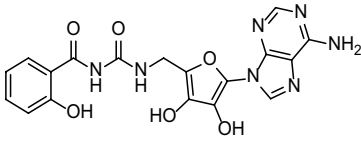
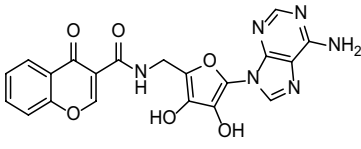
Code	Structure	Compound Details
GV01		IUPAC: ((5-(6-amino-9H-purin-9-yl)-3,4-dihydroxytetrahydrofuran-2-yl)methoxy)(hydroxy)(2-hydroxybenzamido)-14-sulfanolate Chemical Formula: C ₁₇ H ₁₉ N ₆ O ₈ S ⁻ Molecular Weight: 467.43
GV02		IUPAC: N-(N-((5-(6-amino-9H-purin-9-yl)-3,4-dihydroxytetrahydrofuran-2-yl)methyl)sulfamoyl)-2-hydroxybenzamide Chemical Formula: C ₁₇ H ₁₉ N ₇ O ₇ S Molecular Weight: 465.44
GV03		IUPAC: N-((5-(6-amino-9H-purin-9-yl)-3,4-dihydroxytetrahydrofuran-2-yl)methyl)-2-(2-hydroxyphenyl)-2-oxoethane-1-sulfonamide Chemical Formula: C ₁₈ H ₂₀ N ₆ O ₇ S Molecular Weight: 464.45
GV04		IUPAC: N-((5-(6-amino-9H-purin-9-yl)-3,4-dihydroxytetrahydrofuran-2-yl)methyl)-1,1-difluoro-2-(2-hydroxyphenyl)-2-oxoethane-1-sulfonamide Chemical Formula: C ₁₈ H ₁₈ F ₂ N ₆ O ₇ S Molecular Weight: 500.43
GV05		IUPAC: N-((5-(6-amino-9H-purin-9-yl)-3,4-dihydroxytetrahydrofuran-2-yl)methyl)-2-(2-hydroxyphenyl)-2-oxoethane-1-sulfonamide Chemical Formula: C ₁₈ H ₂₀ N ₆ O ₇ S Molecular Weight: 464.45
GV06		IUPAC: N-((5-(6-amino-9H-purin-9-yl)-3,4-dihydroxyfuran-2-yl)methyl)-2-fluoro-N-hydroxybenzamide Chemical Formula: C ₁₇ H ₁₃ FN ₆ O ₅ Molecular Weight: 400.33
GV07		IUPAC: N-(((5-(6-amino-9H-purin-9-yl)-3,4-dihydroxyfuran-2-yl)methyl)carbonyl)-2-hydroxybenzamide Chemical Formula: C ₁₈ H ₁₅ N ₇ O ₆ Molecular Weight: 425.36
GV08		IUPAC: N-((5-(6-amino-9H-purin-9-yl)-3,4-dihydroxyfuran-2-yl)methyl)-4-oxo-4H-chromene-3-carboxamide Chemical Formula: C ₂₀ H ₁₄ N ₆ O ₆ Molecular Weight: 434.37

Table 1 (continued)

GV09		<p>IUPAC: N-((5-(6-amino-9H-purin-9-yl)-3,4-dihydroxytetrahydrofuran-2-yl)methyl)-4-oxo-4H-chromene-3-sulfonamide Chemical Formula: C₁₉H₁₈N₆O₇S Molecular Weight: 474.45</p>
GV10		<p>IUPAC: (5-(6-amino-9H-purin-9-yl)-3,4-dihydroxytetrahydrofuran-2-yl)methyl (2-aminobenzoyl)sulfamate Chemical Formula: C₁₇H₁₉N₇O₇S Molecular Weight: 465.44</p>
GV11		<p>IUPAC: (5-(6-amino-9H-purin-9-yl)-3,4-dihydroxytetrahydrofuran-2-yl)methyl benzoylsulfamate Chemical Formula: C₁₇H₁₈N₆O₇S Molecular Weight: 450.43</p>
GV12		<p>IUPAC: (((5-(6-amino-9H-purin-9-yl)-3,4-dihydroxytetrahydrofuran-2-yl)methoxy)sulfonyl)(5-fluoro-2-hydroxybenzoyl)amide Chemical Formula: C₁₇H₁₆FN₆O₈S Molecular Weight: 483.41</p>
GV13		<p>IUPAC: (5-(6-amino-9H-purin-9-yl)-3,4-dihydroxytetrahydrofuran-2-yl)methoxy)sulfonyl(2-aminophenyl)amide Chemical Formula: C₁₇H₁₈N₇O₈S Molecular Weight: 480.43</p>
GV14		<p>IUPAC: (((5-(6-amino-9H-purin-9-yl)-3,4-dihydroxytetrahydro-1H-furan-1-ium-2-yl)methoxy)sulfonyl)(2-chloronicotinoyl)amide Chemical Formula: C₁₆H₁₆ClN₇O₇S Molecular Weight: 485.86</p>
GV15		<p>IUPAC: N-((5-(6-amino-9H-purin-9-yl)-3,4-dihydroxytetrahydrofuran-2-yl)methyl)-8-hydroxy-4-oxo-4H-chromene-3-sulfonamide Chemical Formula: C₁₉H₁₈N₆O₈S Molecular Weight: 490.45</p>
GV16		<p>IUPAC: N-((5-(6-amino-9H-purin-9-yl)-3,4-dihydroxytetrahydrofuran-2-yl)methyl)-4-oxo-4H-benzo[e][1,2]oxazine-3-sulfonamide Chemical Formula: C₁₈H₁₇N₇O₇S Molecular Weight: 475.44</p>

Table 1 (continued)

GV17		<p>IUPAC: N-((5-(6-amino-9H-purin-9-yl)-3,4-dihydroxytetrahydrofuran-2-yl)methyl)-4-oxo-1,4-dihydroquinoline-3-sulfonamide Chemical Formula: C₁₉H₁₉N₇O₆S Molecular Weight: 473.46</p>
GV18		<p>IUPAC: N-((5-(6-amino-9H-purin-9-yl)-3,4-dihydroxytetrahydrofuran-2-yl)methyl)-4-oxo-1,4-dihydrocinnoline-3-sulfonamide Chemical Formula: C₁₈H₁₈N₈O₆S Molecular Weight: 474.11</p>
GV19		<p>IUPAC: N-((5-(6-amino-9H-purin-9-yl)-3,4-dihydroxytetrahydrofuran-2-yl)methyl)-7-fluoro-4-oxo-1,4-dihydrocinnoline-3-sulfonamide Chemical Formula: C₁₈H₁₇FN₈O₆S Molecular Weight: 492.44</p>
GV20		<p>IUPAC: (((4-(6-amino-9H-purin-9-yl)-2,3-dihydroxycyclopentyl)methoxy)sulfonyl)(2-hydroxybenzoyl)amide Chemical Formula: C₁₈H₁₉N₆O₇S Molecular Weight: 463.45</p>
GV21		<p>IUPAC: (((5-(6-amino-9H-purin-9-yl)-4-hydroxytetrahydrofuran-2-yl)methoxy)sulfonyl)(2-hydroxybenzoyl)amide Chemical Formula: C₁₇H₁₇N₆O₇S Molecular Weight: 449.42</p>
GV22		<p>IUPAC: (((5-(6-amino-9H-purin-9-yl)-4-fluoro-3-hydroxytetrahydrofuran-2-yl)methoxy)sulfonyl)(2-hydroxybenzoyl)amide Chemical Formula: C₁₇H₁₆FN₆O₇S Molecular Weight: 467.41</p>
GV23		<p>IUPAC: (((5-(6-amino-9H-purin-9-yl)-4-fluorotetrahydrofuran-2-yl)methoxy)sulfonyl)(2-hydroxybenzoyl)amide Chemical Formula: C₁₇H₁₆FN₆O₆S Molecular Weight: 451.41</p>
GV24		<p>IUPAC: (N-(((2R,3S,5S)-5-(6-amino-9H-purin-9-yl)-3,4-difluorotetrahydrofuran-2-yl)methyl)sulfamoyl)(2-hydroxybenzoyl)amide Chemical Formula: C₁₇H₁₆F₂N₇O₅S Molecular Weight: 468.42</p>

Table 1 (continued)

GV25		<p>IUPAC: N-(N-(((2S,3R,4R,5R)-5-(6-amino-9H-purin-9-yl)-3,4-difluorotetrahydrofuran-2-yl)methyl)sulfamoyl)-2-hydroxybenzamide Chemical Formula: C₁₇H₁₇F₂N₇O₅S Molecular Weight: 469.42</p>
GV26		<p>IUPAC: (((5-(4-amino-1H-indol-1-yl)-3,4-dihydroxytetrahydrofuran-2-yl)methoxy)sulfonyl)(2-hydroxybenzoyl)amide Chemical Formula: C₂₀H₂₀N₃O₈S⁻ Molecular Weight: 462.45</p>
GV27		<p>IUPAC: (((3,4-dihydroxy-5-(6-oxido-9H-purin-9-yl)tetrahydrofuran-2-yl)methoxy)sulfonyl)(2-hydroxybenzoyl)amide Chemical Formula: C₁₇H₁₅N₅O₉S²⁻ Molecular Weight: 465.39</p>
GV28		<p>IUPAC: (((5-(6-(cyclopropylamino)-9H-purin-9-yl)-3,4-dihydroxytetrahydrofuran-2-yl)methoxy)sulfonyl)(2-hydroxybenzoyl)amide Chemical Formula: C₂₀H₂₁N₆O₈S⁻ Molecular Weight: 505.48</p>
GV29		<p>IUPAC: (((5-(6-amino-2-(phenylamino)-9H-purin-9-yl)-3,4-dihydroxytetrahydrofuran-2-yl)methoxy)sulfonyl)(2-hydroxybenzoyl)amide Chemical Formula: C₂₃H₂₂N₇O₈S⁻ Molecular Weight: 556.53</p>
GV30		<p>IUPAC: (((5-(6-amino-2-cyclohexyl-9H-purin-9-yl)-3,4-dihydroxytetrahydrofuran-2-yl)methoxy)sulfonyl)(2-hydroxybenzoyl)amide Chemical Formula: C₂₃H₂₇N₆O₈S⁻ Molecular Weight: 547.56</p>
GV31		<p>IUPAC: (((5-(6-amino-2-phenyl-9H-purin-9-yl)-3,4-dihydroxytetrahydrofuran-2-yl)methoxy)sulfonyl)(2-hydroxybenzoyl)amide Chemical Formula: C₂₃H₂₁N₆O₈S⁻ Molecular Weight: 541.52</p>

Table 1 (continued)

GV32		<p>IUPAC: N-((5-(6-(cyclopropylamino)-9H-purin-9-yl)-3,4-dihydroxytetrahydrofuran-2-yl)methyl)sulfamoyl)(2-hydroxybenzoyl)amide Chemical Formula: C₂₀H₂₂N₇O₇S⁻ Molecular Weight: 504.50</p>
GV33		<p>IUPAC: N-((5-(6-(cyclopropylamino)-2-phenyl-9H-purin-9-yl)-3,4-dihydroxytetrahydrofuran-2-yl)methyl)sulfamoyl)(2-hydroxybenzoyl)amide Chemical Formula: C₂₆H₂₆N₇O₇S⁻ Molecular Weight: 580.60</p>
GV34		<p>IUPAC: N-((5-(6-amino-2-phenyl-9H-purin-9-yl)-4-fluoro-3-hydroxytetrahydrofuran-2-yl)methyl)sulfamoyl)(2-hydroxybenzoyl)amide Chemical Formula: C₂₃H₂₁N₇O₆S⁻ Molecular Weight: 542.52</p>
GV35		<p>IUPAC: (((5-(4-amino-6-(naphthalen-1-yl)-1H-[1,2,3]triazolo[4,5-c]pyridin-1-yl)-3,4-dihydroxytetrahydrofuran-2-yl)methoxy)sulfonyl)(2-hydroxybenzoyl)amide Chemical Formula: C₂₇H₂₃N₆O₈S⁻ Molecular Weight: 591.58</p>
GV36		<p>IUPAC: (((5-(4-amino-6-(4-(trifluoromethyl)phenyl)-1H-[1,2,3]triazolo[4,5-c]pyridin-1-yl)-3,4-dihydroxytetrahydrofuran-2-yl)methoxy)sulfonyl)(2-hydroxybenzoyl)amide Chemical Formula: C₂₄H₂₀F₃N₆O₈S⁻ Molecular Weight: 609.51</p>
GV37		<p>IUPAC: N-(N-(((2R,5R)-5-(6-amino-9H-purin-9-yl)-3,4-dihydroxytetrahydrofuran-2-yl)methyl)-N-methylsulfamoyl)-2-hydroxybenzamide Chemical Formula: C₁₈H₂₁N₇O₇S Molecular Weight: 479.47</p>
GV38		<p>IUPAC: N-(N-(((2R,5R)-3,4-dihydroxy-5-(6-methoxy-9H-purin-9-yl)tetrahydrofuran-2-yl)methyl)sulfamoyl)-2-hydroxybenzamide Chemical Formula: C₁₈H₂₀N₆O₈S Molecular Weight: 480.45</p>

Overlay methods Herein, the ligand's docked conformation was overlaid with its bioactive crystallized conformation.

Chemical resemblance Herein, the process involves mimicking the specific ligand binding process within the active binding site of the receptor as it occurs in the biological cellular system in terms of interacting residues [51].

Binding site identification and grid box generation

The binding site/active site for both proteins was identified by using the position of the internal ligand and the interacting residues of the individual macromolecules with the help of the AutoDock 4.2.6 program. The identified binding site was further utilized to specify the grid parameter points required to generate a 3D grid box. In both proteins, the grid box was located by considering the internal ligand as a center and wrapping each of the macromolecular residues interacting with the ligand to ensure that every possible ligand conformation falls inside the grid box [52]. The grid box dimensions used are mentioned in Table 2. The AutoGrid 4.2 was executed by providing the AutoGrid executable, and *gpf* files as input and were converted to the grid log file (*.glg*). It generated map files for different types of atoms present in the ligand as well as the receptor. In this study, A C Cl F Br I HD N NA OA SA, etc., map files were generated by AutoGrid 4.2 [53]. The generated map files were utilized by the AutoDock 4.2.6 program for carrying out molecular docking simulations.

Protein–ligand docking

All molecular docking simulation studies were performed using the AutoDock 4.2.6 program (ADP) [54]. After the successful execution of AutoGrid 4.2, the genetic algorithm was set to default. Lamarckian genetic algorithm (LGA) produces a trail population of various ligand conformations followed by mutational conformations and swapping different parameters relating to successive generations of biological evaluations for the final selection of a bioactive confirmation with the lowest binding energy. In addition to it, individual and selective conformational search for their local conformational space, and identification of local minima, is an additional characteristic of the Lamarckian algorithm [53]. LGA was used for search parameters [55]. For particular

proteins, the semi-empirical force field was used to predict the ligand's binding energy. The machine-generated docking parameter file (DPF) contains the numerous parameters required for each ligand docking in the protein's active site [52]. Parameters were as follows: the number of genetic algorithm (GA) runs was set to 50, with 2,500,000 evaluations and population size of 150. AutoDock 4.2 executable was used to run molecular docking of each ligand, and *dpf* files as input were converted to the docking log file (*.dlg*). The final *.dlg* file offers binding energies for every run and inhibition constant along with a clustering histogram. From the histogram, low-energy conformer from the largest cluster was selected. This low-energy conformer of top-scoring molecules was then taken for further analysis. Complex files for binding mode analysis and for further MD simulations were then generated using the data from the *.dlg* file and the protein *.pdbqt* files. The protein–ligand complex interactions were then visualized in 2D/3D using UCSF Chimera 1.16 [47] and BIOVIA Discovery Studio Visualizer program [42].

Molecular dynamics simulation study

MDS helps study the protein–ligand complex's structural stability and flexibility. In this study, MDS was performed for the top hit compound to legitimize the protein–ligand complex (PLC) and measure the ligand-binding constancy in the active site of the selected target. MDS was carried out using the Desmond module of Schrodinger Suite developed by the D. E. Shaw Research group (academic license) [41]. Through the system's builder panel, the orthorhombic simulation box was prepared with the simple point-charge (SPC) explicit water model. A minimum distance of 10 Å was maintained between the protein and the solvent surface. Protein–ligand docked complexes were solvated using the cubic SPC water model [56]. The solvated system was then neutralized with counter ions and physiological salt (0.15 M). The receptor–ligand complex system was designated with the OPLS AA force field [57]. A hybrid energy minimization algorithm with 1000 steps of the steepest descent followed by conjugate gradient algorithms was utilized for energy minimization of the PLC. The reversible reference system propagator algorithm (RESPA) integrator [58], the Nosé–Hoover chain thermostat [59], and the Martyna–Tobias–Klein barostat were used with two ps relaxation times. The equilibrated PLC system (1RT2-GV17 and 7BV2-GV17) was used for the final production of

Table 2 Details of grid parameters used in the current study

Protein ID	Center grid box dimensions (Å)			Spacing (Å)	Coordinates for the center of the grid box		
	x-axis	y-axis	z-axis		x-axis	y-axis	z-axis
1RT2	40	40	40	0.375	−3.782	−35.698	24.873
7BV2	60	60	60	0.375	91.776	91.56	104.863

the MD simulation for 100 ns at 310.15 K temperatures at 1.0 bar pressure with NPT (isothermal–isobaric ensemble [60], i.e., constant temperature, constant pressure, constant number of particles) ensemble while using default settings for relaxation before simulation. The trajectory files were written. The *_out.cms* file was imported to view the trajectories for further exploration. To understand the stability of the complex during MD simulation, the protein backbone frames were aligned to the backbone of the initial frame. Finally, the simulated interaction diagram was analyzed by loading the *_out.cms* file and selected RMSD to obtain the mentioned plots below [61]. To perform the post-simulation MM-GBSA analysis of GV17 with both proteins, the *thermal_MMGBSA.py script* of the Prime/Desmond module of the Schrodinger Suite was used (Schrodinger; institute license) [62]. The post-simulation MM-GBSA analysis of free binding energy calculation was carried out with the generation of 0–1000 frames. A total of 200 frames were processed and analyzed throughout the MM-GBSA calculation of 100-ns MDS data. The binding energy calculation was performed on the basis of this parameter: MM-GBSA ΔG_{bind} , the binding energy of the receptor and ligand as calculated by the prime energy, a molecular mechanics + implicit solvent energy function (kcal/mol).

ADME and toxicity prediction

Absorption, distribution, metabolism, and excretion (ADME) is a pharmacokinetic/pharmacodynamic process that defines how the body reacts to a drug. *In silico* ADME data supports the drug development process as it helps in lead optimization [63]. In this study, based on molecular docking and dynamics results, the identified potential hit molecule was subjected to predictive ADME evaluation using SwissADME (an online web server developed and maintained by the Swiss Institute of Bioinformatics (SIB) (<https://www.swissadme.ch>)) [64]. The structures of ligands were drawn individually in the Marvin JS input

panel provided on the website (<http://swissadme.ch/index.php>), or the SMILES format can be uploaded. After the final run, the server predicted *in silico* ADME. It is necessary to assess a drug's safety profile to predict the *in silico* toxicity. Despite determining the harmful levels in animals, they also help reduce the number of animal tests. In the present study, we have used the pkCSM web server to predict the pharmacokinetic properties of our small molecules using graph-based signatures [65]. This server database provides the following toxicity details: AMES toxicity, maximum tolerated dose, hepatotoxicity, skin sensitization, and hERG I and II inhibition.

Results

Molecular docking studies

Validation of docking procedure

The validation/redocking studies on the crystal structure of HIV-1 RT (PDB ID: 1RT2) and RdRp of SARS-CoV-2 (PDB ID: 7BV2) revealed the binding energy of -11.62 kcal/mol and -8.70 kcal/mol with a K_i value of 3.04 nM and 422.25 nM and the reference RMSD of 0.54 Å and 1.24 Å. These minor RMSD fluctuations are acceptable for small molecules (0–3 Å). The overlay conformations of both internal ligands concerning their crystallized conformation are presented in Fig. 1.

Docking-based virtual screening

All ligands' docking investigation with RdRp from SARS-CoV-2 main protease and HIV-1 RT revealed favorable binding energies and inhibition constants. Also, as an observation, it was seen that nearly 30% of the ligands showed a better binding affinity than the reference/internal ligand; this shows how well the ligands fitted into the sub-pockets of RdRp-SARS-CoV-2 and HIV-1 RT. Considering the top four scoring molecules/top hits (Figs. 2, 3, 4, 5, 6, 7,

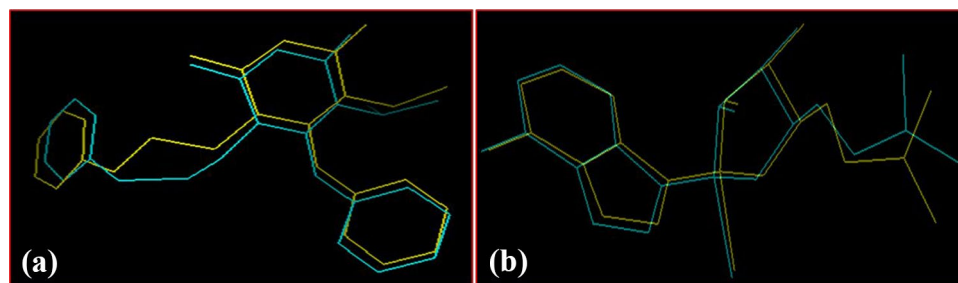


Fig. 1 The superimposed overlay conformation of the docked internal ligand **a** TNK concerning its crystallized conformation obtained from the co-crystallized complex structure (PDB: 1RT2) and **b** F56 con-

cerning its crystallized conformation obtained from the co-crystallized complex structure (PDB: 7BV2)

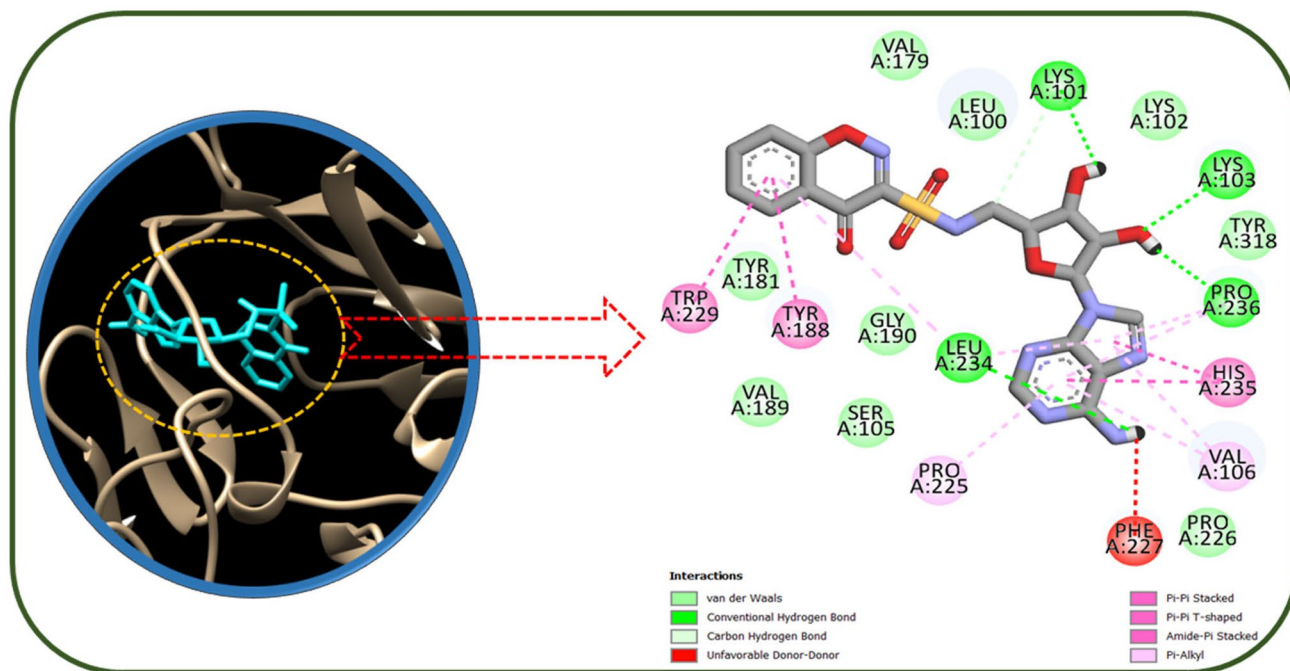


Fig. 2 Docking interaction of GV16 (MbtA inhibitor) in the binding pocket of IRT2 showing various interactions within the active site

8, and 9), only GV17 was found to bind effectively with both the proteins (IRT2 and 7BV2) with binding energies of -12.64 kcal/mol and -9.44 kcal/mol and inhibition constants (K_i) of 546.25 pM and 121.22 nM, respectively. The

binding energies/docking scores and inhibition constants of all molecules are presented in Table 3. Tables 4 and 5 show the interaction details of the top four ligands with HIV-1 RT (PDB ID: 1RT2) and RdRp-SARS-CoV-2 (PDB ID: 7BV2).

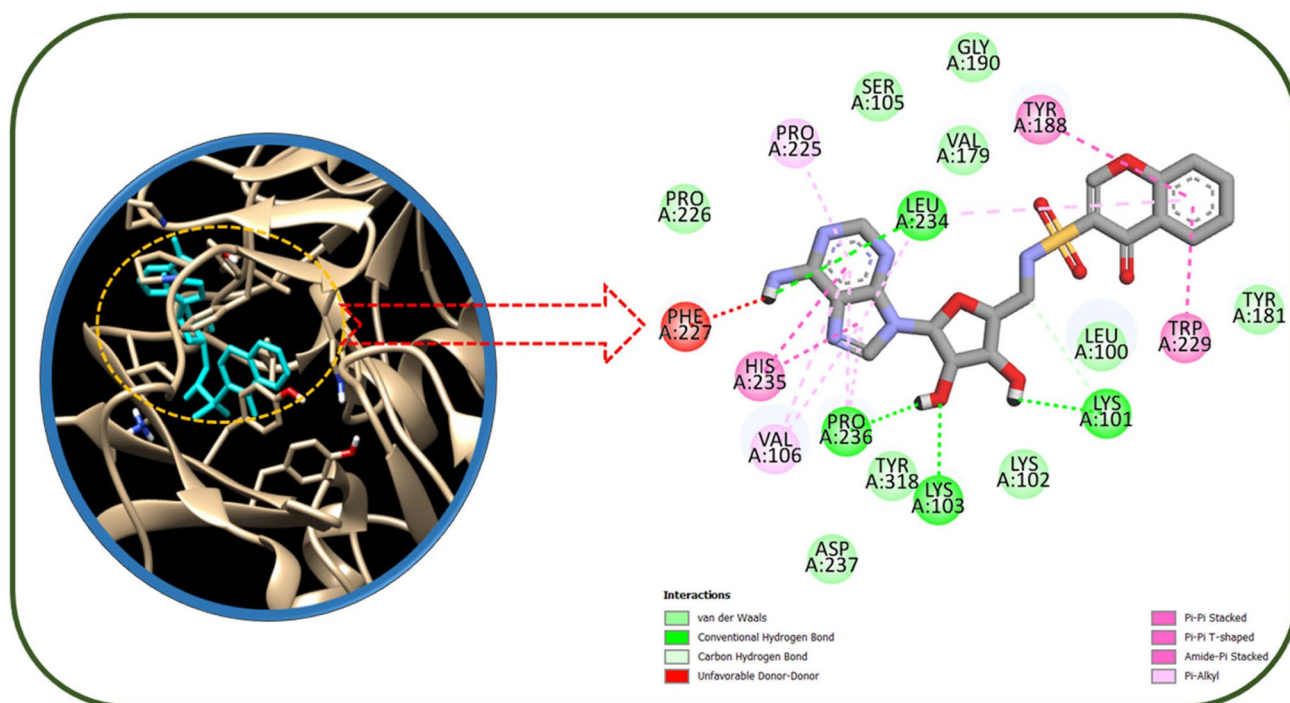


Fig. 3 Docking interaction of GV09 (MbtA inhibitor) in the binding pocket of IRT2 showing various interactions within the active site

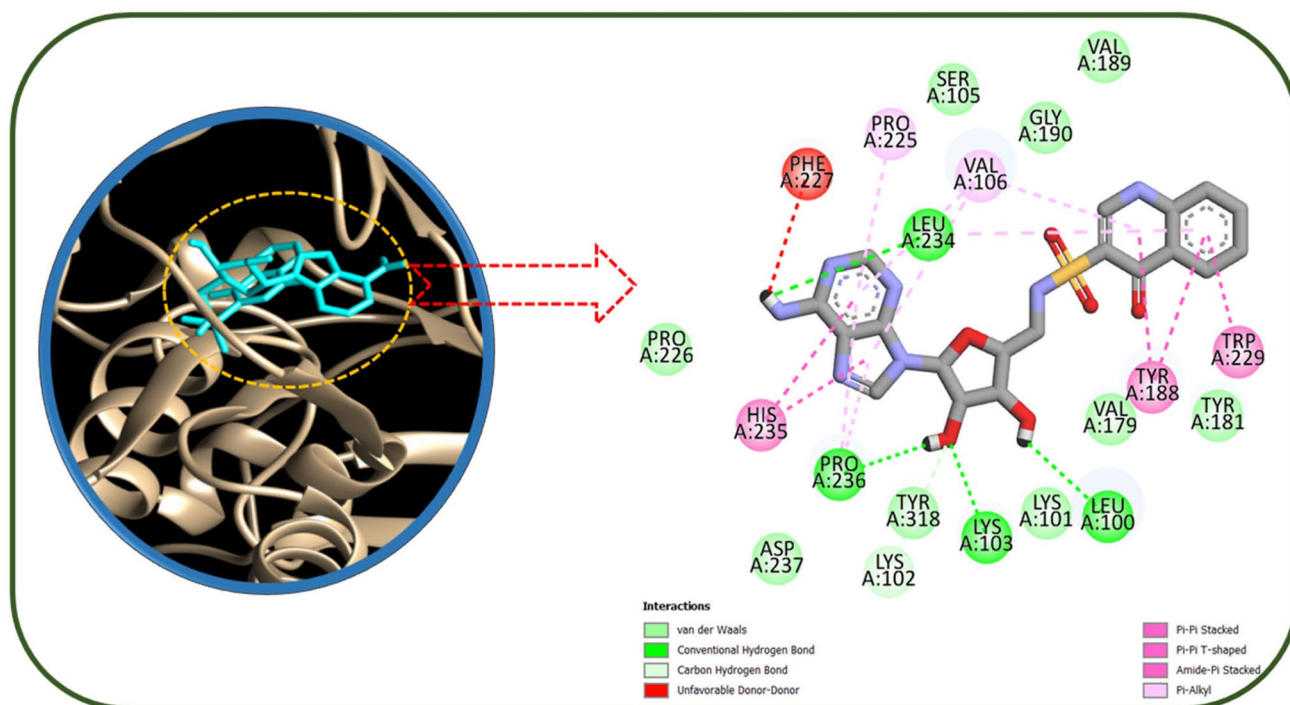


Fig. 4 Docking interaction of GV17 (MbtA inhibitor) in the binding pocket of IRT2 showing various interactions within the active site

Molecular docking interaction analysis

Since we are focusing on finding a triple co-infection inhibitor, it is crucial to have a detailed study on the interactions

observed to develop a proof of concept. Among the top dock score molecules, the detailed visual pose view analysis has been performed for GV17 as it was seen to interact with both the proteins (IRT2 and 7BV2) efficiently.

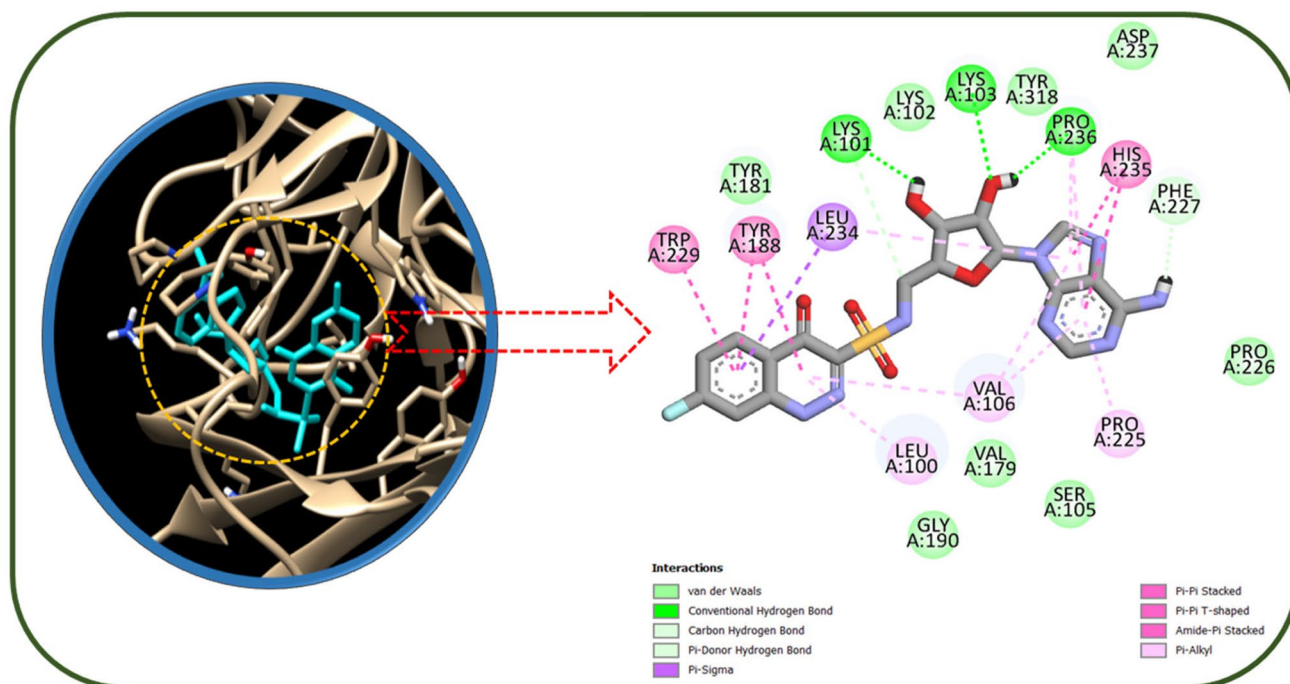


Fig. 5 Docking interaction of GV19 (MbtA inhibitor) in the binding pocket of IRT2 showing various interactions within the active site

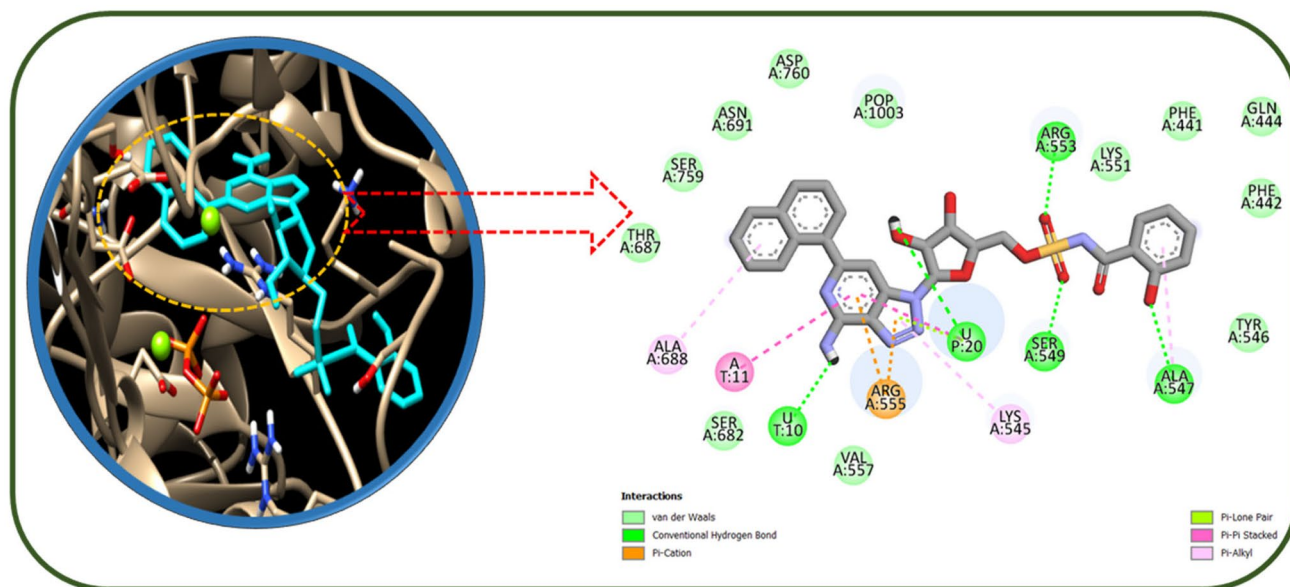


Fig. 6 Docking interaction of GV35 (MbtA inhibitor) in the binding pocket of 7BV2 showing various interactions within the active site

HIV-1 reverse transcriptase (PDB ID: 1RT2)–GV17 complex Nucleoside reverse transcriptase inhibitors (NRTIs) and non-nucleoside reverse transcriptase inhibitors (NNRTIs) are the two basic types of reverse transcriptase inhibitors (RTIs). The former act as chain terminators, and the latter act by impeding DNA synthesis. Nucleotide RTIs also contribute to the inhibition program as their mode of action is the same as that of NRTIs. The reported MbtA inhibitors are modified nucleotides and hence interact well with 1RT2.

Moreover, the docking score of GV17 was more than that of the reference compound TNK 651. Due to the apparent critical function of reverse transcriptase in HIV replication, suppressing this enzyme is one of the most promising targets for AIDS treatment. GV17 showed a significant interaction with active site amino acid residues and H bond interactions with the critical amino acid residues. This binding pocket has the advantage of high potency, selectivity, specificity, and low toxicity. The active site pocket is mainly a hydrophobic

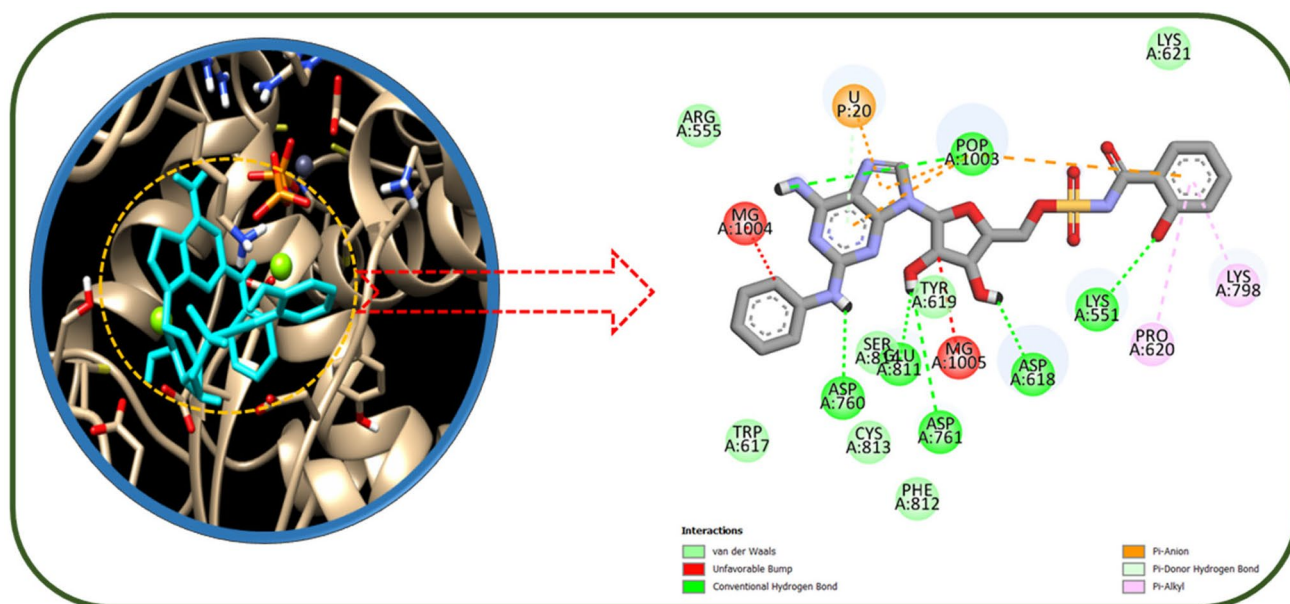


Fig. 7 Docking interaction of GV29 (MbtA inhibitor) in the binding pocket of 7BV2 showing various interactions within the active site

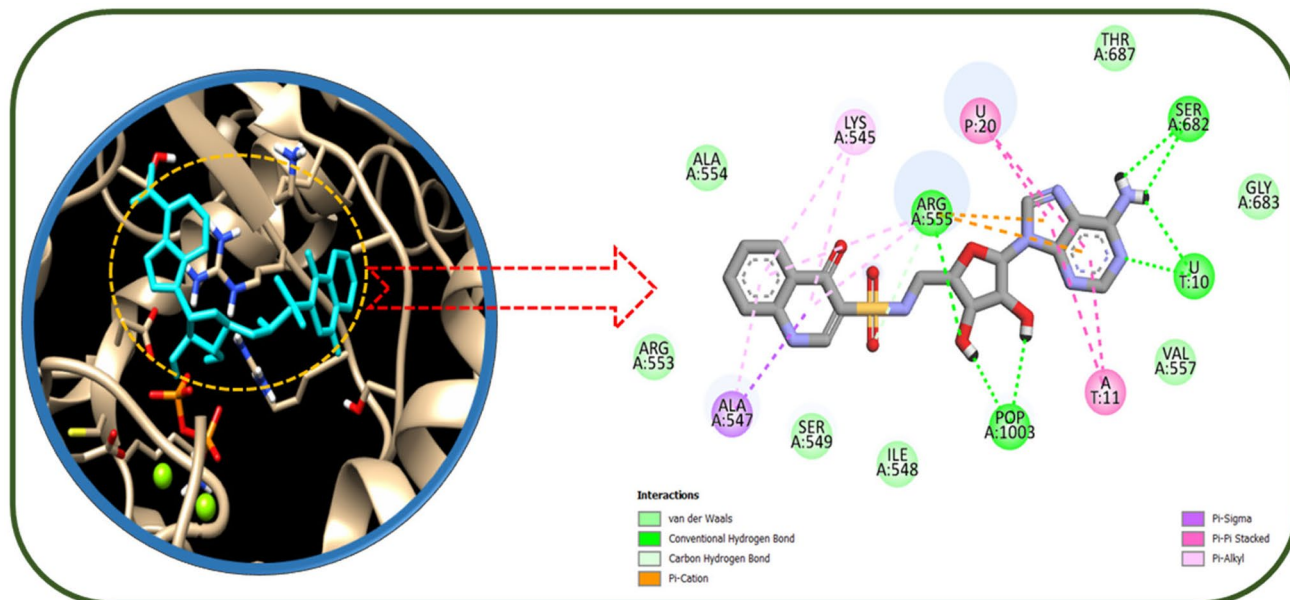


Fig. 8 Docking interaction of GV17 (MbtA inhibitor) in the binding pocket of 7BV2 showing various interactions within the active site

pocket comprising side chains of aromatic amino acid residues (Tyr181, Trp229, Tyr188, Phe227, and Tyr318) and hydrophobic amino acid residues (Pro95, Leu100, Val106, Val108, Val179, Leu234, and Pro236 from the p66 subunit). The HIV protein binding site also contains the following essential residues: Lys101A, Tyr 101A, Leu 100A, Val 106A, Tyr 188A, Tyr 181A, Val 179A, and Glu 138B. GV17 was favorably embedded in the hydrophobic pocket surrounded by the side chains of Leu 100A, Val 106A,

Val 189A, Val 179, Leu 234A, Pro 236A, Ser 105A, Gly 190A, Pro 226A, Asp 237A, and Lys102A. It also had four hydrogen bond interactions: Leu 234A with an amino group ($-NH_2$) present in the purine ring and Pro 236A, Lys103A, and Leu 100A with the hydroxy groups ($-OH$) present in tetrahydrofuran-3,4-diol. The presence of a more significant number of H bonds leads to the effective binding of the ligand in the active site. Regarding the internal ligand, the π - π stacking interactions (attractive, non-covalent

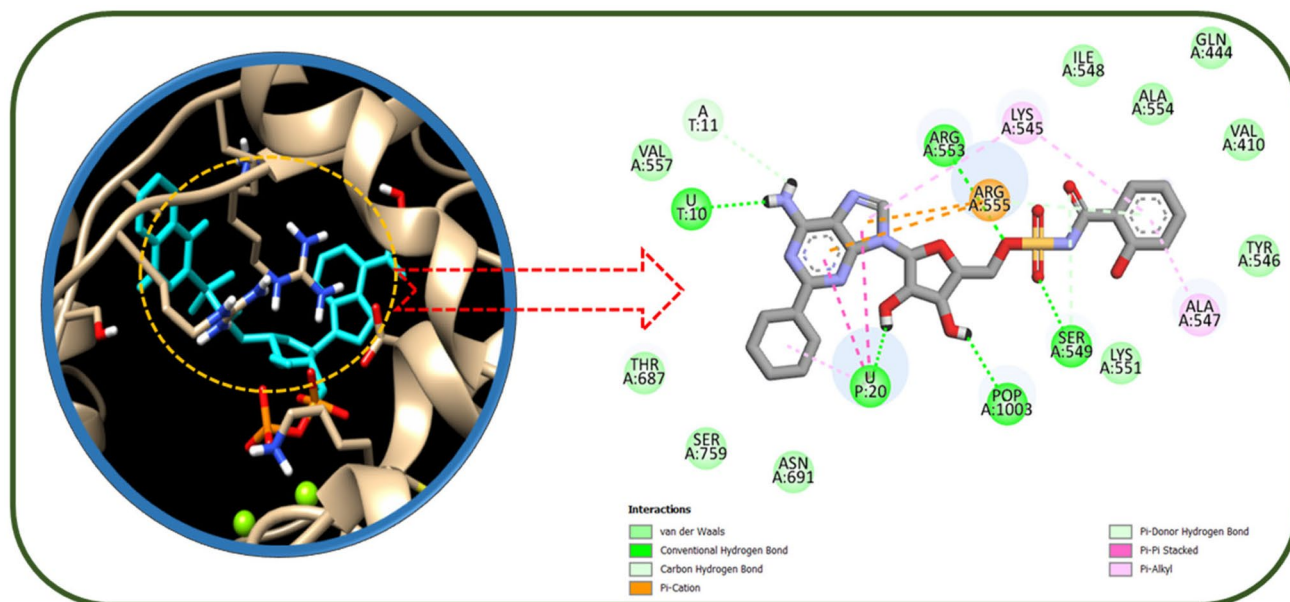


Fig. 9 Docking interaction of GV30 (MbtA inhibitor) in the binding pocket of 7BV2 showing various interactions within the active site

Table 3 Results of molecular docking study of 38 analogues (MbtA inhibitors) against HIV-1 reverse transcriptase (PDB ID: 1RT2) and RNA-dependent RNA polymerase from SARS-CoV-2 (PDB ID: 7BV2) arranged in order of best score

S. no.	Code	Largest cluster (PDB ID: 1RT2)		Code	Largest cluster (PDB ID: 7BV2)	
		Binding energy (kcal/mol)	Inhibition constant (K_i)		Binding energy (kcal/mol)	Inhibition constant (K_i)
1	Reference	−11.62	3.04 nM	Reference	−8.70	422.25 nM
2	GV16	−12.93	330.07 pM	GV35	−9.69	78.52 nM
3	GV09	−12.69	497.68 pM	GV29	−9.51	106.78 nM
4	GV17	−12.64	546.25 pM	GV17	−9.44	121.22 nM
5	GV19	−12.62	562.28 pM	GV30	−9.33	144.88 nM
6	GV18	−12.61	571.65 pM	GV33	−9.27	160.21 nM
7	GV35	−11.96	1.72 nM	GV09	−9.2	179.25 nM
8	GV15	−11.92	1.82 nM	GV16	−9.16	193.06 nM
9	GV11	−11.7	2.65 nM	GV26	−9.08	219.49 nM
10	GV26	−11.47	3.90 nM	GV08	−9.01	248.36 nM
11	GV10	−11.19	6.29 nM	GV34	−8.88	308.66 nM
12	GV27	−11.1	7.34 nM	GV15	−8.46	632.70 nM
13	GV14	−11.09	7.4 nM	GV18	−8.45	634.88 nM
14	GV21	−10.84	11.39 nM	GV14	−8.4	696.64 nM
15	GV23	−10.75	13.09 nM	GV10	−8.35	762.59 nM
16	GV04	−10.71	14.15 nM	GV02	−8.17	1.03 μM
17	GV12	−10.69	14.71 nM	GV23	−8.17	1.02 μM
18	GV02	−10.55	18.49 nM	GV36	−8.15	1.06 μM
19	GV05	−10.33	26.76 nM	GV11	−8.07	1.21 μM
20	GV07	−10.19	34.05 nM	GV19	−8.02	1.33 μM
21	GV31	−10.16	35.42 nM	GV12	−8.01	1.34 μM
22	GV34	−10.16	35.84 nM	GV07	−7.98	1.41 μM
23	GV06	−10.12	38.14 nM	GV28	−7.94	1.51 μM
24	GV08	−10.06	42.00 nM	GV21	−7.85	1.77 μM
25	GV30	−10.06	41.92 nM	GV31	−7.66	2.44 μM
26	GV24	−10.03	44.25 nM	GV13	−7.4	3.74 μM
27	GV03	−10.02	45.52 nM	GV22	−7.39	3.84 μM
28	GV32	−9.95	51.12 nM	GV32	−7.34	4.17 μM
29	GV22	−9.93	52.99 nM	GV05	−7.29	4.57 μM
30	GV28	−9.86	59.17 nM	GV37	−7.19	5.38 μM
31	GV13	−9.85	60.06 nM	GV03	−7.18	5.42 μM
32	GV36	−9.78	67.34 nM	GV06	−7.1	6.30 μM
33	GV25	−9.42	124.19 nM	GV20	−7.05	6.82 μM
34	GV20	−9.36	137.28 nM	GV25	−7.03	6.99 μM
35	GV33	−9.36	136.76 nM	GV38	−6.99	7.55 μM
36	GV38	−9.26	162.43 nM	GV04	−6.97	7.76 μM
37	GV01	−8.87	315.27 nM	GV01	−6.79	10.47 μM
38	GV29	−8.19	990.55 nM	GV24	−6.58	15.10 μM
39	GV37	−2.85	8.14 mM	GV27	8.19	989.47 nM

interactions between aromatic rings) were conserved in GV17: Trp 229A and Tyr 188A with the quinolin-4(1*H*)-one ring and His 235A with the 9*H*-purine ring. It helps in understanding the intrinsic nature of the molecular assembly. The repositioning of Tyr 181A to form favorable van der Waals interactions is essential. The Pro 236A loops

flex to optimize contacts with the substrate, which may suffice for the stability of the ligand (GV17). The loops move partly as rigid bodies leaving a residual pocket partially occupied by an electron-dense group that appears to form a hydrogen bond with the hydroxyl oxygen of the residue Lys103A. These interactions may be responsible for the

Table 4 Details of the docking interaction of top-scoring analogues (MbtA inhibitors) with the interacting residues in the binding pocket of HIV-1 reverse transcriptase (PDB ID: 1RT2) along with H bond length (Å)

Sl. no.	Code	(PDB ID: 1RT2) docking interactions	H bond distance (Å)
01	GV16	(H bond)-Lys101, Lys103, Pro236, & Leu234, (Pi-Pi stacking)-His235, Tyr188, Trp229, (Pi-Alkyl)-Val106, & Pro225, (van der Waals)-Val179, Leu100, Lys102, Tyr318, Pro226, Ser105, Gly190, Val189, & Tyr181	1.77, 1.99, 2.10, & 1.97
02	GV09	(H bond)-Lys101, Lys103, Pro236, & Leu234, (Pi-Pi stacking)-His235, Tyr188, Trp229, (Pi-Alkyl)-Val106, & Pro225, (van der Waals)-Val179, Leu100, Lys102, Tyr318, Pro226, Ser105, Gly190, Asp237, & Tyr181	1.92, 1.92, 2.05, & 2.05
03	GV17	(H bond)-Lys101, Lys103, Pro236, & Leu234, (Pi-Pi stacking)-His235, Tyr188, Trp229, (Pi-Alkyl)-Val106, & Pro225, (van der Waals)-Val179, Lys102, Tyr318, Pro226, Ser105, Gly190, Val189, Tyr181, Asp237, & Lys101	1.96, 2.14, 2.03, & 3.08
04	GV19	(H bond)-Lys101, Lys103, & Pro236, (Pi-Pi stacking)-His235, Tyr188, Trp229, (Pi-Alkyl)-Val106, Leu100, & Pro225, (van der Waals)-Val179, Lys102, Tyr318, Pro226, Ser105, Gly190, Phe227, & Tyr181	1.93, 2.07, & 1.75

binding affinity of the molecule, as indicated by the docking scores of -12.47 kcal/mol compared to the reference ligand Tnk 651. Hence, the total volume of the active site is exploited, and the conformation is the stabilized presence of a compact inhibitor (GV17). Thus, from the binding mode analysis and docking studies, it can be concluded that GV17 with a tetrahydrofuran moiety flanked with purine moiety and quinolinone ring, which have been substituted with electron-donating and electron-withdrawing groups, showed a significant affinity towards HIV-1 reverse transcriptase compared to the reference drug TNK 651. Thus, this type of nucleotide scaffold could be exploited to develop novel HIV-1 RT inhibitors, which can facilitate better patient adherence and inhibit resistant strains of HIV.

RNA-dependent RNA polymerase from SARS-CoV-2 (PDB ID: 7BV2)–GV17 complex Identifying potential molecules that can disrupt the functionalities of critical proteins of the SARS-CoV-2 machinery can be used as a line of defense against nCOVID-19. Apart from 3CL main protease, RdRp is a target protein in SARS-CoV-2 that has been validated

and extensively studied for drug development in nCOVID-19 as it shares a high degree of homology between SARS-CoV and MERS-CoV. It has highly conserved active catalytic motifs. Due to the crucial role of RdRp in viral replication, it is considered an essential target for designing, developing, and repurposing antiviral compounds against nCOVID-19. Nucleotide drugs like ribavirin, favilavir, and remdesivir can inhibit SARS-CoV-2 *in vitro* [66]. GV17, a nucleotide analogue, could be a promising therapeutic moiety as nucleotide analogues have shown promising activity in various earlier studies [67, 68]. The docking score of GV17 (-9.44 kcal/mol) was more than that of the reference compound F58 (-8.70 kcal/mol). GV17 interacted with RdRp amino acid residues via a predominant metal coordination bond and hydrogen bonding with the active site. It revealed conserved interactions with the active site as that of remdesivir. It had formed four hydrogen bonds with RdRp pocket residues: Arg 555A and POP 1003A with hydroxy groups (-OH) present in tetrahydrofuran-3,4-diol, Ser 682A with an amino group (-NH₂) present in purine ring, U 10 T (uridine base) with an amino group (-NH₂) present in purine ring, and the N

Table 5 Details of the docking interaction of top-scoring analogues (MbtA inhibitors) with the interacting residues in the binding pocket of nCOVID-19 RdRp (PDB ID: 7BV2) along with H bond length (Å)

Sl. no.	Code	(PDB ID: 7BV2) docking interactions	H bond distance (Å)
01	GV35	(H bond)-Arg553, Ser549, & Ala547, (hydrogen-bonded bases)-U10 & U20, (Pi-Pi stacking)-A11, (Pi-Alkyl)-Ala688 & Lys545, (van der Waals)-Asp760, Asn691, Ser759, Thr687, Ser682, Val557, Tyr546, Phe442, Gln, 444, Phe441, Lys551, & POP1003	2.31, 2.00, 2.60, 2.44, & 2.65
02	GV29	(H bond)-Asp760, Asp761, Glu811, Asp618, & Lys551, (hydrogen-bonded bases)-POP1003, (Pi-Alkyl)-Pro620 & Lys798, (van der Waals)-Lys621, Arg555, Trp617, Cys813, Phe812, Tyr619, & Ser814	1.81, 2.08, 3.03, 1.77, 2.03, & 2.38
03	GV17	(H bond)-Arg555 & Ser682, (hydrogen-bonded bases)-U10 & POP1003, (Pi-Pi stacking)-A11 and U20, (Pi-Alkyl)-Lys545, (van der Waals)-Ala554, Arg553, Ser549, Ile548, Val557, Gly683, & Thr687	2.12, 2.29, 2.32, & 2.10
04	GV30	(H bond)-Arg553 & Ser549, (hydrogen-bonded bases)-U10, U20 & POP1003, (Pi-Cation)-Arg555, (Pi-Alkyl)-Ala547 & Lys545, (van der Waals)-Val557, Thr687, Ser759, Asn691, Lys551, Tyr546, Val410, Ala554, Gln444, & Ile548	2.10, 2.52, 2.03, 2.95, & 2.04

heteroatom in purine ring. The hydrogen bonding with the uridine base leads to a stable complex formation, as has been observed with remdesivir. The two extra hydrogen bonds (Arg 555A and Ser 682A) may explain the apparent higher potency of GV17 in inhibiting SARS-CoV-2 replication as it stabilizes the incoming nucleotide in the correct position for catalysis. Further, GV17 was covalently linked to the primary strand in protein structure to the pyrophosphate moiety and three magnesium as catalytic ions, as observed in remdesivir monophosphate. With reference to remdesivir, the π - π stacking interactions (attractive, non-covalent interactions between aromatic rings) were conserved in GV17: U 20P (uridine base) and A 11 T with the 9*H*-purine ring. It helps in understanding the intrinsic nature of molecular assembly [69].

Molecular dynamics simulations and post-MM-GBSA analysis

Molecular dynamics simulation studies were carried out for GV17-HIV-1 RT and GV17-RdRp-SARS-COV-2 to test the constancy of the ligand binding in the active site of the selected targets. MD studies are implemented in many drug discovery applications to study the nature of macromolecules or to interpret mechanisms of drug resistance [70]. The obtained simulation findings are discussed below.

HIV-1 reverse transcriptase (PDB ID: 1RT2)-GV17 complex

In this target protein, the conformations revealed significant RMSD values of 4.2 Å, indicating that the protein–ligand

complexes were maintained constantly throughout the simulation time. RMSD explains the structural confirmations throughout the simulation. From Fig. 10, it can be interpreted that the protein–ligand complex revealed maximum stability after a 22-ns simulation with a combined RMSD of 4.2 Å (protein) and 4.2 Å (ligand). For small biomolecules, this fluctuation was acceptable. Because possible effective inhibitors should be able to bind strongly to the enzyme and create stable non-dynamic complexes, the dynamicity property provides a valid criterion to evaluate the efficiency of a proposed inhibitor.

As illustrated in Fig. 11, the hydrogen bond interactions were maximum during the simulation. The amino acid residues Lys-103, Leu-234, Tyr-318, Glu-138, and Pro-236 exhibited hydrogen bond contact with GV17; interestingly, the same amino acid residue was observed in the protein's docked pose with the ligand (Lys-103, Leu-234, Pro236, and Leu-100) (Fig. 4). Figure 12 shows the detailed atomic interactions of ligand GV17 with the protein residues of PDB-1RT2. It shows the amino acid residues involved in the bond formation with GV17 in the active site of 1RT2. This suggests that the protein–ligand complex remained stable throughout the simulation, and the system's backbone fluctuations were modest. The simulation demonstrated more hydrophobic contacts and water-mediated linkages with GV17; the MD simulations also revealed amino acid-mediated water bridges. Figure 13 represents the specific contacts made by the protein with the ligand throughout the MD simulation. The darker the color, the greater the number of linkages with the amino acid.

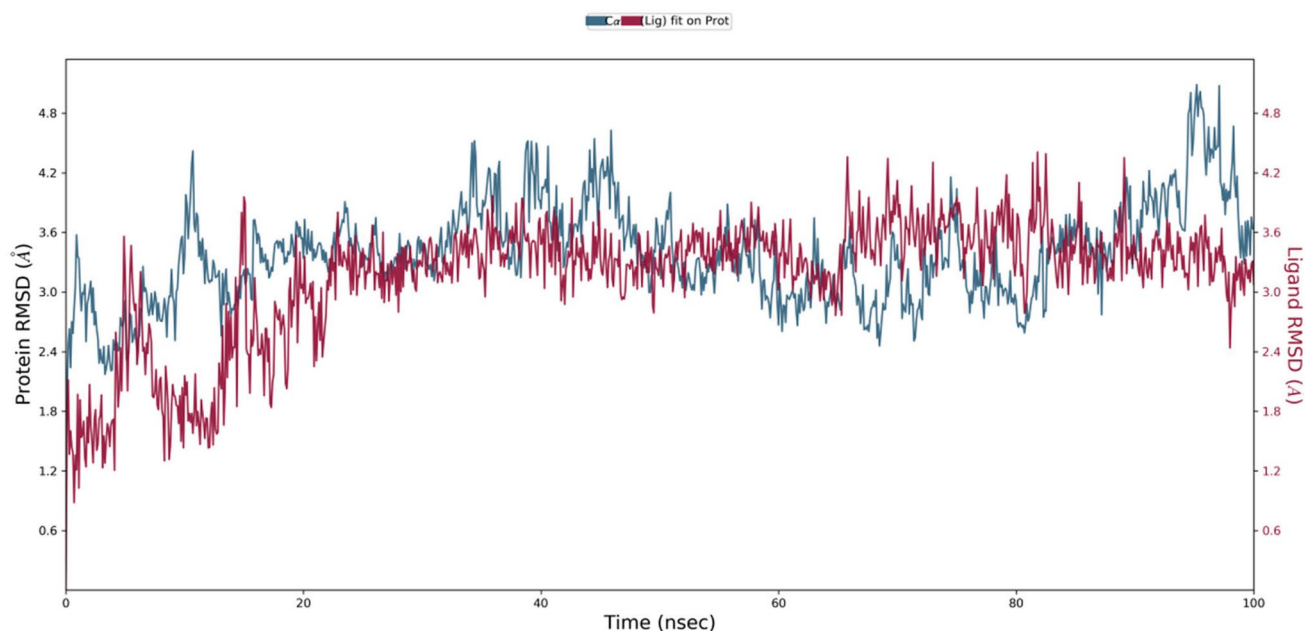
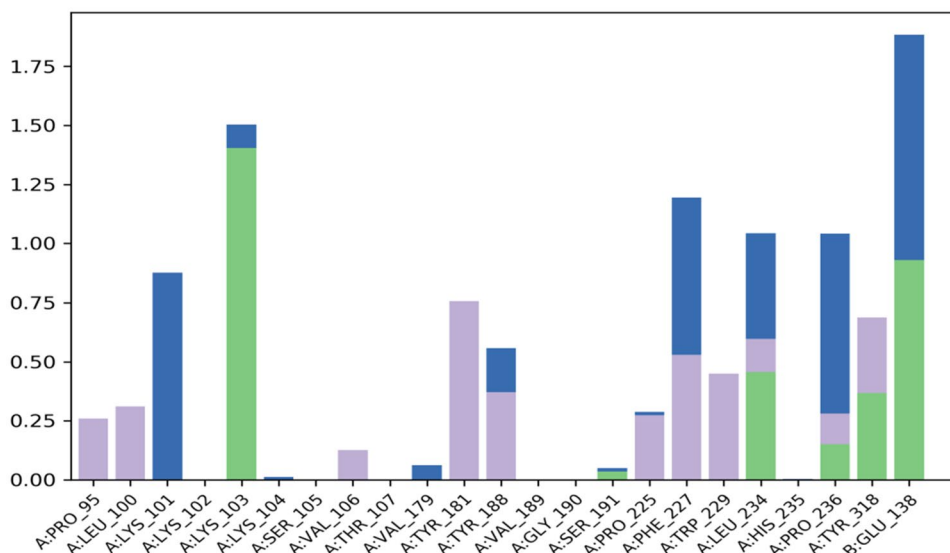


Fig. 10 Root mean square deviation (RMSD) of the protein–ligand complex of 1RT2 with the lowest binding energy compound GV17

Fig. 11 Plot (stacked bar charts) of protein interactions with the ligand supervised throughout the molecular dynamics simulation of the 1RT2-GV17 complex system



RNA-dependent RNA polymerase from SARS-CoV-2 (PDB ID: 7BV2)–GV17 complex

Any viral polymerase enzyme's function is to replicate the virus genome or polyproteins, necessitating much flexibility in the active site to accommodate both the template and the replicate [71]. The polymerases described so far are relatively dynamic and have a large active site [72]. In this study, the computed RMSD of the protein was 2.40 Å, respectively, showing the SARS-COV-2 RNA-dependent RNA polymerase's less dynamic characteristics. Also,

because possible effective inhibitors should be able to bind strongly to the enzyme and create stable non-dynamic complexes, this dynamicity provides a valid metric to evaluate the efficacy of a potential inhibitor. It is well evident from Fig. 14 that the protein–ligand complex was stable after the 10-ns simulation with a combined RMSD of 2.4 Å (protein) and 4.5 Å (ligand).

As illustrated in Fig. 15, the hydrogen bond interactions were maximum during the simulation. The amino acid residues Tyr-619, Cys-622, Thr-680, Ser-681, Asn-691, and Asp-760 exhibited hydrogen bond contact with GV17. Figure 16 shows the detailed atomic interactions of ligand GV17 with the protein residues of PDB-7BV2. This suggests that the protein–ligand complex remained stable throughout the simulation, and the system's backbone fluctuations were modest. The simulation demonstrated more hydrophobic contacts and water-mediated linkages with GV17; the MD simulations also revealed amino acid–mediated water bridges. Figure 17 represents the specific contacts made by the protein with the ligand throughout the MD simulation. The darker the color, the greater the number of linkages with the amino acid.

The robust binding capacity of GV17 and the numerous contacts created between GV17 and its target proteins under study may account for its possible inhibitory activity. Thus, our MD studies revealed the complexes' exceptional stability for both proteins. Furthermore, the H bond study demonstrates that the H bonds remained stable throughout the simulation and would likely play a substantial role in complex stabilization.

The calculated binding free energy, ΔG average of the molecule GV17, was found to be -72.30 ± 7.85 kcal/mol and -65.40 ± 7.25 kcal/mol for 1RT2 and 7BV2, respectively.

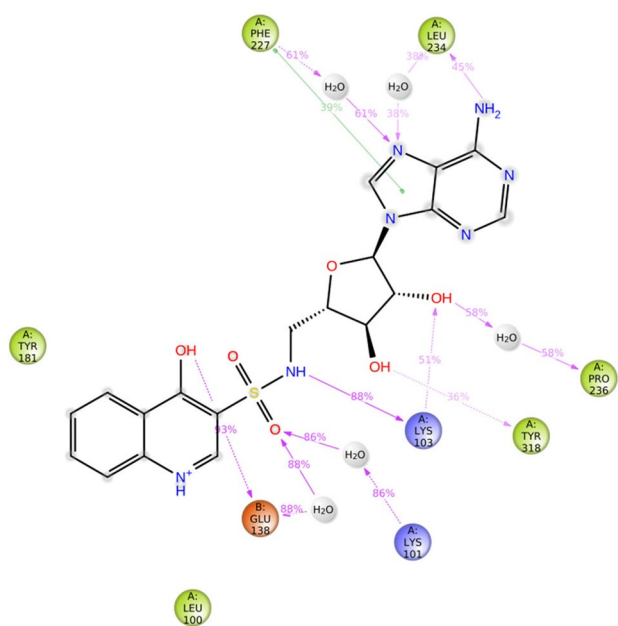
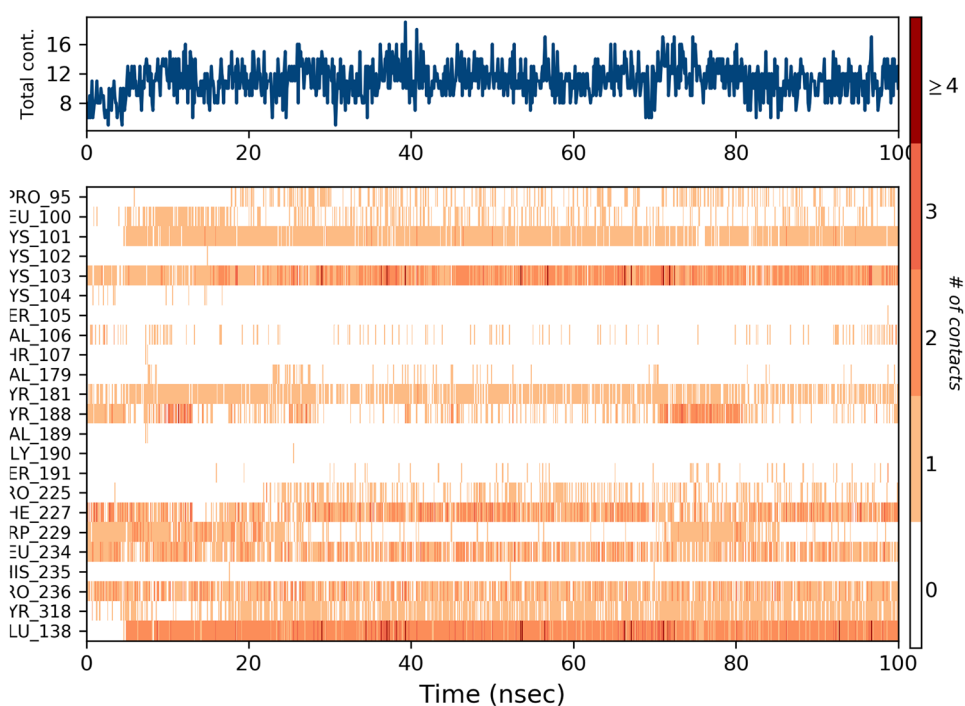


Fig. 12 Detailed ligand GV17 atomic interactions with the protein residues of PDB-1RT2

Fig. 13 Specific contacts made by the protein with the ligand throughout the trajectory. (Dark color indicates more specific contact with the ligand)



The more negative binding energy indicates a stronger affinity of GV17 towards both the receptors.

Thus, based on the above interaction analysis of GV17 with HIV-1 RT and RdRp from SARS-CoV-2 main protease and the

MM-GBSA data, it is clear that the MbtA inhibitor (GV17) could serve the purpose of solving triple co-infection cases. GV17, being a modified nucleotide analogue, interacts much more efficiently with both the proteins. To sum up, GV17

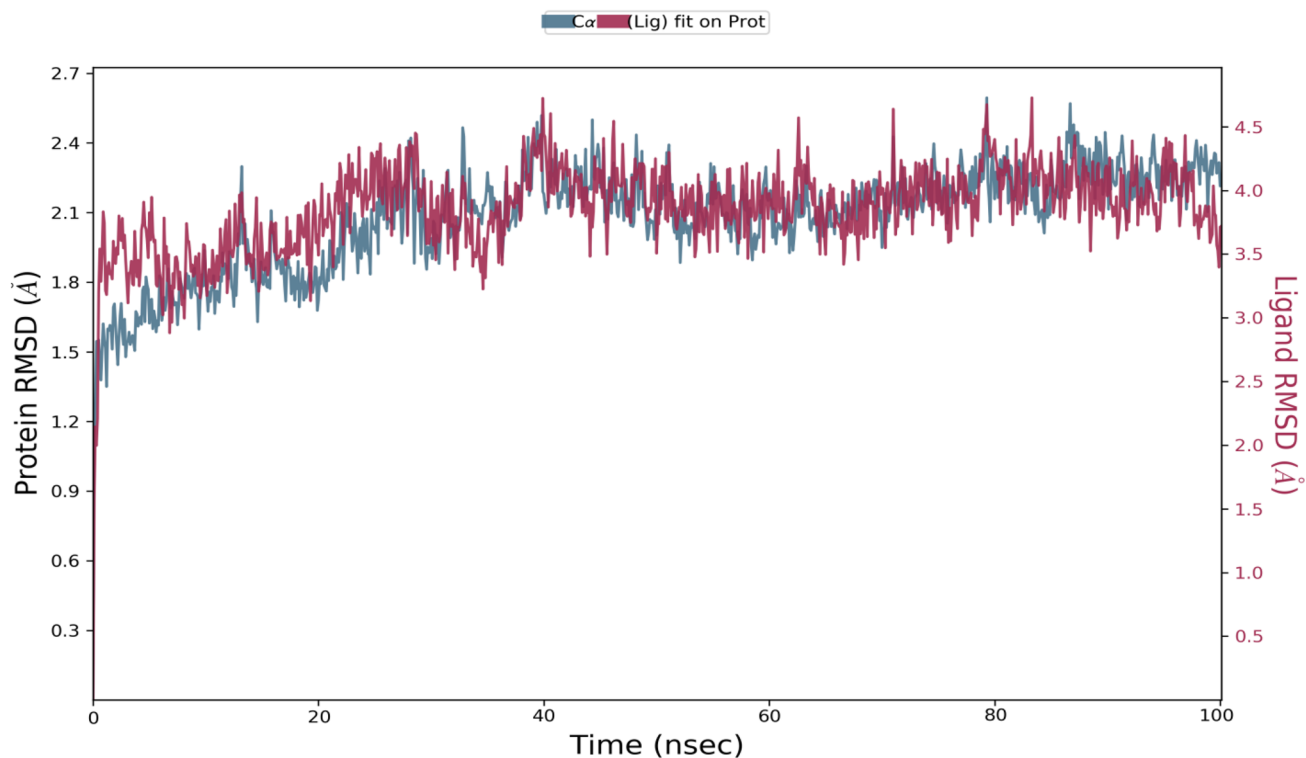
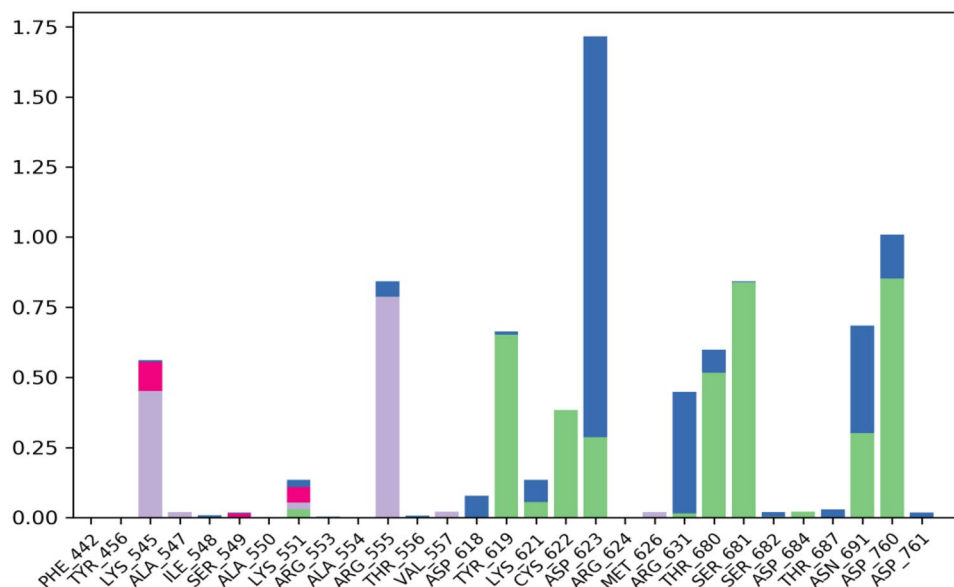


Fig. 14 Root mean square deviation (RMSD) of the protein–ligand complex of 7BV2 with the lowest binding energy compound GV17

Fig. 15 Plot (stacked bar charts) of protein interactions with the ligand supervised throughout the molecular dynamics simulation of the 7BV2-GV17 complex system



could have good efficacy against RdRp from SARS-CoV-2 and HIV-1 RT when tested experimentally. Significantly, it has the potential to block the critical residues of both the receptors, as discussed above.

ADME and toxicity prediction

Results of drug-likeness, bioavailability, synthetic feasibility, and alerts for PAINS and Brenk filters

GV17 was subjected to ADME predictive evaluation using SwissADME. Drug-likeness predicts the possibility of a

molecule transforming into an oral drug. In our study, five filters were employed to calculate the drug-likeness. GV17 exhibited moderate violation of drug-likeness and had a bioavailability score (55%). The Abbot Bioavailability Score predicts the fate of a molecule for 10% oral bioavailability (in rats) or quantifiable Caco-2 cell line permeability experiment. It may be defined by a feasibility score of 11%, 17%, 56%, and 85%. GV17 exhibited a score of 55%, suggesting a good bioavailability. PAINS and Brenk methods were employed to recognize the possible uncertain fragments that yield false-positive biological output. The studies indicated that GV17 did not violate any of the criteria. The synthetic

Fig. 16 Detailed ligand GV17 atomic interactions with the protein residues of PDB-7BV2

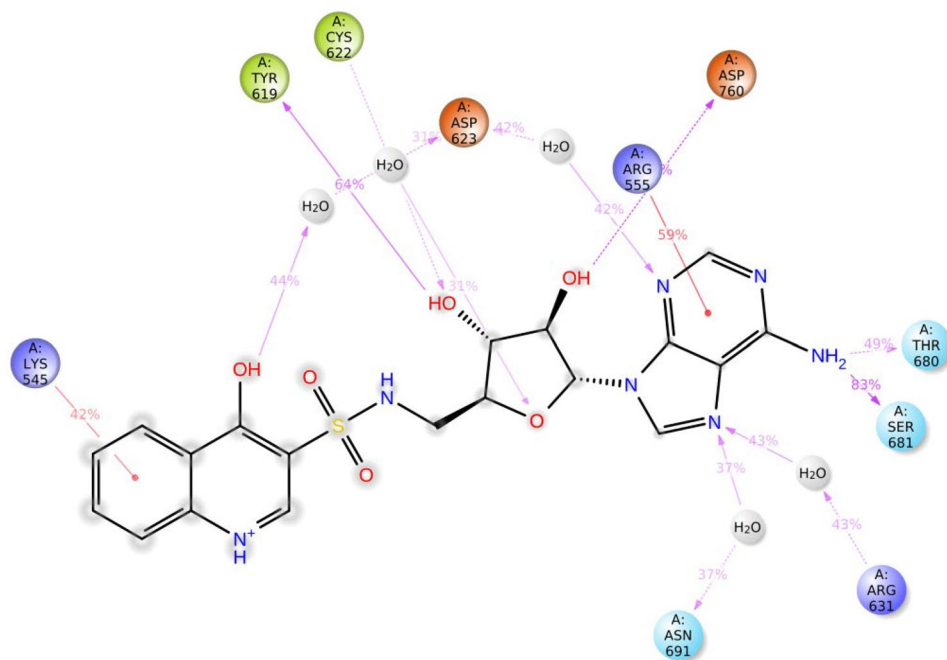
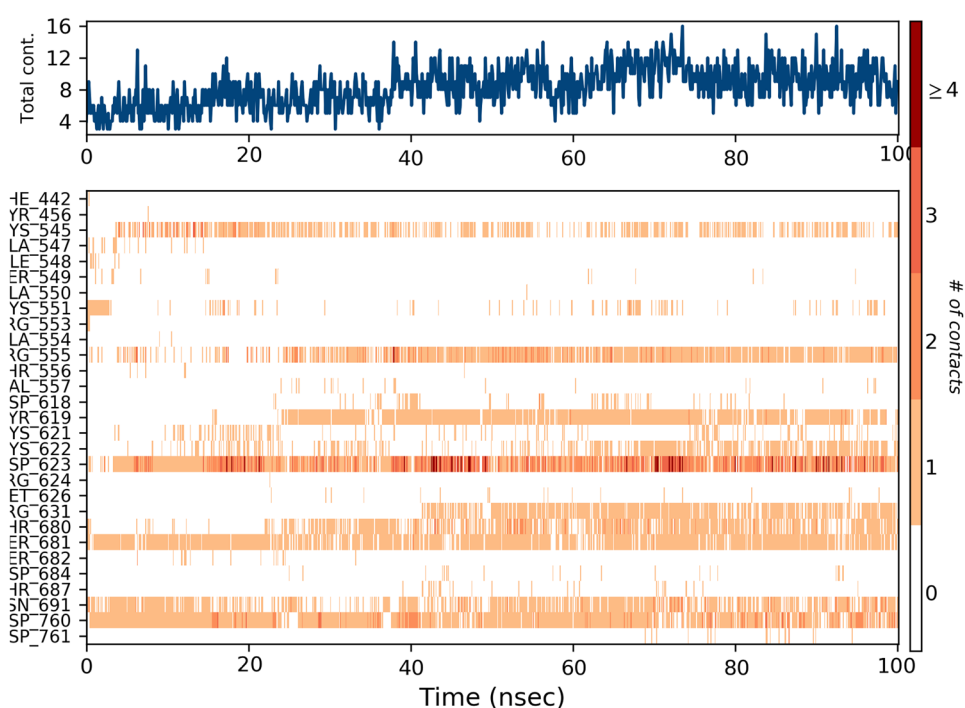


Fig. 17 Specific contacts made by the protein with the ligand throughout the trajectory. (Dark color indicates more specific contact with the ligand)



accessibility of GV17 showed a moderate level of toughness as per protocols (on a scale of 1 (easy) to 10 (extremely tough)). Detailed analysis is shown in Table 6.

In silico evaluation for pharmacokinetics compliance

The fate of a molecule in the human body is evaluated in terms of its ADME properties. The ADME parameters of GV17 were estimated by calculating the different physico-chemical and biopharmaceutical parameters. The physico-chemical features of GV17 were analyzed.

The results indicated that the molar refractivity, which accounts for the overall polarity of the molecules, was 115; this value was in the acceptable range of the standard values (30–140). The topological polar surface area (TPSA) was 206.72 Å². These data suggest that the molecules cannot cross the blood–brain barrier (BBB). Solubility class lipophilicity refers to the capacity of a molecule to dissolve itself into a lipophilic medium and correlates to various representations of drug properties that affect ADMET, including permeability; absorption, distribution, metabolism, and excretion; solubility; plasma protein binding; and toxicity. Results of iLOGP and Silicos-it suggested that the iLOGP value 1.20 was in the acceptable range (−0.4 to +5.6), while the Silicos-it value −1.18 was in the favorable range. This lead molecule had an excellent intestinal absorption profile (48%). Water solubility is an important parameter affecting a drug's absorption and distribution. Log *S* calculations

represent the molecule's solubility in water at 25 °C. For adequate solubility, the calculated log *S* values through the ESOL model should not exceed 6. GV17 showed a log *S* value of −2.96, accounting for good solubility. The data above suggests that GV17 had a good balance between permeability and solubility and might show a good bio-availability upon oral drug administration. The predicted GI absorption was low.

Permeability predictions help understand the outcomes of ADMET and the cell-based bioassays. Results showed that the permeability over human skin was −9.09 cm/s which was in the acceptable range. GV17 did not show the properties to cross the BBB, as discussed earlier. Metabolism can sometimes lead to drug–drug interaction and affect the bioavailability of drugs. Only the free form of the drug can bind with drug-metabolizing enzymes. To study the metabolic behavior of our lead compounds, it is vital to study their interaction with cytochrome P450 enzymes (CYPs), as they are the most notable class of metabolizing enzymes. The lead compounds found were assessed for their CYPs' (CYPs of human liver microsomes (HLMs)) inhibitory activity. Detailed analyses are given in Table 7.

Toxicity prediction

Analogue GV17 was studied in detail for its *in silico* toxicity profile. AMES test, which helps identify the mutagenic potential of a chemical compound using bacteria,

Table 6 Tabular representation of different drug-likeness rules, bioavailability, synthetic accessibility, and alerts for PAINS and Brenk

S. no.	Code	Drug-likeness rules					Alerts		Synthetic accessibility	
		Lipinski (Pfizer)	Ghose (Amgen)	Veber (GSK)	Egan (Pharmacia)	Muegge (Bayer)	Bioavailability score	PAINS		Brenk
1	GV17	Yes	Yes	No	No	No	0.55	0	0	4.75

Table 7 Details of the *in silico* ADMET profile of GV17 using the SwissADME online server

Code of compounds	GV17
ADMET profile	
Physicochemical parameters	
Formula	C19H19N7O6S
Molecular weight	473.46 g/mol
Mol. refractivity	115.06
TPSA	206.72 Å ²
Lipophilicity	
ILOGP	1.20
Silicos-it	-1.18
Water solubility	
Log S (ESOL), class	-2.96 (soluble)
Pharmacokinetics	
GI absorption	Low
Intestinal absorption (human)	47.606
BBB permeant	No
Log K _p (skin perm.)	-9.09 cm/s
CYP1A2	No
CYP2D6	No

showed favorable results as it showed no AMES toxicity. Results suggested that the maximum tolerated dose (human) was 0.326 log mg/kg/day, representing a moderate dosage level as per protocols. Results revealed that these compounds showed no hERG1 (human ether-a-go-go-related gene) inhibition, negating the probability of ventricular arrhythmia. The oral rat acute toxicity (LD₅₀) value was 2.401 mol/kg, while the oral rat chronic toxicity (LOAEL) value was 3.037, indicating a good safety profile. It showed neither hepatotoxicity nor skin sensitization. The predicted toxicity results of analogues GV17 are mentioned in Table 8.

Table 8 Tabular representation data of predicted toxicity-identified leads

Model name	Units	Code GV17
AMES toxicity	Yes/no	No
Max. tolerated dose (human)	Log mg/kg/day	0.326
hERG I inhibitor	Yes/no	No
Oral rat acute toxicity (LD50)	mol/kg	2.401
Oral rat chronic toxicity (LOAEL)	Log mg/kg bw/day	3.037
Hepatotoxicity	Yes/no	No
Skin sensitization	Yes/no	No
<i>Tetrahymena pyriformis</i> toxicity	Log µg/L	0.285
Minnow toxicity	Log mM	-0.836

Conclusion

The co-existence of various diseases poses a significant threat to humanity. The rationale for performing this study was to repurpose the antitubercular drugs (MbtA inhibitors) for their effectiveness against HIV-RT and RdRp from SARS-COV-2. This also aimed to prevent the side effects of excessive medication in triple co-infection cases due to the administration of multiple drugs and multiple-dose regimens. The primary objective was to find a multi-targeted ligand/inhibitor that would show strong affinity with both the protein targets. The fact that these MbtA inhibitors were nucleotides gained our attention as we are in search for a chemical scaffold to target an appropriate vital protein in pathogens causing tuberculosis, HIV/AIDS, and nCOVID-19 infections/co-infections. The substrates for HIV-1 RT and RdRp of nCOVID-19 were invariably nucleotides, and hence, an appropriately designed nucleotide analogue could have affinity towards all the three target proteins. In the anticipation to combat these triple co-infections by finding a multi-targeted ligand herein, we had employed the concepts of structure-based virtual screening (SBVS) widely employed in drug discovery and repurposing. With regard to SBVS approaches, molecular docking results suggested that GV17 was the only molecule that interacted strongly with the active site residues of both proteins and successfully established various interactions, mostly hydrogen bonding. GV17 could mimic most of the interactions, as in the case of internal ligands in both proteins. Moreover, the binding energy achieved by GV17 was more than that of internal ligands, which indicates a very strong binding in the active site pocket. To validate molecular docking results, molecular dynamic simulations (100 ns) of both the PLCs (1RT2-GV17 and 7BV2-GV17) were run to evaluate and improve our design concept. The results suggested that GV17 had the potential to bind effectively in the active site of both proteins. Both PLCs were found to be stable, as is evident from the observed RMSD profile. The overall simulated structure does not exhibit any significant conformation changes and remains close to the experimental structures. Both the bioactive molecules under study stayed in the binding pocket during the simulation and formed many stable hydrophobic, polar, and H bond interactions, as discussed. This confirms the stability of GV17 in the binding pocket of both proteins. Herein, we have supported the MD simulation with the binding free energy calculations as it reflects the amount of the energy released during complex formation. A relatively stable protein–ligand complex displays more negative binding energy, indicating a stronger ligand affinity towards its receptor. We observed a similar pattern of ΔG for both our PLCs. The predicted *in silico* ADMET profile of GV17 was satisfactory. However, there remains scope for

improving the pharmacokinetic profile of GV17 by an active analogue approach. However, we faced severe limitations while comparing three different sets of diseases belonging to different pathological situations. Also they lack phylogenetic correlation. The research on this concept is at a very nascent stage, and hence, lack of literature on this very idea made things more complex but, at the same time allowed us to explore and generate specific hypotheses, which we further tried to validate through *in silico* studies. The goal of this study was to not only find a promising triple co-infection inhibitor/multi-targeted ligand but also to pave a pathway for future nCOVID-19, TB, and HIV-1 RT drug development. Our findings can open a new avenue to fight against nCOVID-19-HIV-TB infection simultaneously using a single drug moiety.

Future vision

This study aimed to identify a potential triple co-infection inhibitor/multi-targeted ligand for the deadly TB, nCOVID-19, and HIV co-infection through a structure-based drug design approach. Although we have identified a possible multi-targeted inhibitor for RdRp of SARS-CoV-2 and HIV-1 RT, through the *in silico* approach, much work is to be done before the identified HIT (GV17) reaches clinical trials. However, we have identified the crucial residues and types of bonds required to block the RdRp of SARS-CoV-2 and HIV-1 RT, the same needs to be validated through *in vitro* studies. It is indeed worth thinking about improving the ADMET profile and drug-likeness. Based on the findings of this investigation, we will pursue more structure-based drug design methodologies in the future to develop a lead chemical suitable for clinical trials for the treatment of nCOVID-19 also; hence, it could be concluded that the future scope of this study depends on the *in vitro* response of GV17 against HIV-1 RT and RdRp of SARS-CoV-2.

Acknowledgements Gourav Rakshit is thankful to the Birla Institute of Technology, Mesra, Ranchi, India, for providing (i) financial support (Institute Research Fellowship dated March 1, 2021), (ii) the necessary infrastructural support, and (iii) computational facilities (Schrödinger) to perform the simulations.

Author contribution All authors contributed to the study conception and design. Material preparation, data collection, computational work, and analysis were performed by Gourav Rakshit. The first draft of the manuscript was written by Gourav Rakshit, and all authors commented on previous versions of the manuscript. Venkatesan Jayaprakash supervised, reviewed, and edited all the manuscript versions. All authors read and approved the final manuscript.

Funding This work received financial support from the Birla Institute of Technology, Mesra, Ranchi, India, provided to Gourav Rakshit in the form of Institute Research Fellowship (IRF) dated March 1, 2021.

Data availability The datasets generated during and/or analyzed during the current study are available from the corresponding author on reasonable request.

Declarations

Competing interests The authors declare no competing interests.

References

- World Health Organization (2022) Smallpox. https://www.who.int/health-topics/smallpox#tab=tab_1. Accessed 14 Jun 2022
- World Health Organization (2022) Plague. https://www.who.int/health-topics/plague#tab=tab_1. Accessed 14 Jun 2022
- World Health Organization (2022) Malaria. <https://www.who.int/news-room/fact-sheets/detail/malaria>. Accessed 14 Jun 2022
- World Health Organization (2022) Influenza seasonal. https://www.who.int/health-topics/influenza-seasonal#tab=tab_1. Accessed 14 Jun 2022
- World Health Organization (2022) Tuberculosis. https://www.who.int/health-topics/tuberculosis#tab=tab_1. Accessed 14 Jun 2022
- World Health Organization (2022) HIV/AIDS. <https://www.who.int/news-room/fact-sheets/detail/hiv-aids>. Accessed 14 Jun 2022
- World Health Organization (2022) Cholera. <https://www.who.int/news-room/fact-sheets/detail/cholera>. Accessed 14 Jun 2022
- World Health Organization (2022) Rabies. <https://www.who.int/news-room/fact-sheets/detail/rabies>. Accessed 14 Jun 2022
- World Health Organization (2022) Pneumonia. <https://www.who.int/news-room/fact-sheets/detail/pneumonia>. Accessed 14 Jun 2022
- World Health Organization. Ebola virus disease. <https://www.who.int/news-room/fact-sheets/detail/ebola-virus-disease>. Accessed 14 Jun 2022
- Centre for Disease Control and Prevention (2022) Variant Creutzfeldt-Jakob disease. <https://www.cdc.gov/prions/vcjd/index.html>. Accessed 14 Jun 2022
- World Health Organization. Marburg virus disease. https://www.who.int/health-topics/marburg-virus-disease#tab=tab_1. Accessed 14 Jun 2022
- World Health Organization. Middle East respiratory syndrome-coronavirus-mers#tab=tab_1. https://www.who.int/health-topics/middle-east-respiratory-syndrome-coronavirus-mers#tab=tab_1. Accessed 14 Jun 2022
- World Health Organization. Dengue and severe dengue. <http://www.who.int/mediacentre/factsheets/fs117/en/>. Accessed 14 Jun 2022
- World Health Organization. Yellow fever. <https://www.who.int/news-room/fact-sheets/detail/yellow-fever>. Accessed 14 Jun 2022
- Centre for Disease Control and Prevention (2022) Hantavirus. <https://www.cdc.gov/hantavirus/index.html>. Accessed 14 Jun 2022
- Centre for Disease Control and Prevention (2022) Anthrax. <https://www.cdc.gov/anthrax/index.html>. Accessed 14 Jun 2022
- Centre for Disease Control and Prevention (2019) Methicillin-resistant Staphylococcus aureus (MRSA). [https://www.cdc.gov/mrsa/index.html#:~:text=Methicillin-resistantStaphylococcus aureus \(MRSA\)isacauseof,work%2Candgotoschool](https://www.cdc.gov/mrsa/index.html#:~:text=Methicillin-resistantStaphylococcus aureus (MRSA)isacauseof,work%2Candgotoschool). Accessed 14 Jun 2022
- Centre for Disease Control and Prevention (2022) Pertussis (whooping cough). <https://www.cdc.gov/pertussis/index.html>. Accessed 14 Jun 2022
- World Health Organization (2022) Tetanus. https://www.who.int/health-topics/tetanus#tab=tab_1. Accessed 14 Jun 2022
- World Health Organization (2022) Meningitis. https://www.who.int/health-topics/meningitis#tab=tab_1. Accessed 14 Jun 2022
- Centers for Disease Control and Prevention (2022) Syphilis. <https://www.cdc.gov/std/syphilis/stdfact-syphilis-detailed.htm>. Accessed 14 Jun 2022
- World Health Organization (2022) Severe Acute Respiratory-Syndrome (SARS). https://www.who.int/health-topics/severe-acute-respiratory-syndrome#tab=tab_1. Accessed 14 Jun 2022
- World Health Organization (2022) Leprosy. <https://www.who.int/news-room/fact-sheets/detail/leprosy>. Accessed 14 Jun 2022
- World Health Organization (2022) Measles. <https://www.who.int/news-room/fact-sheets/detail/measles>. Accessed 14 Jun 2022
- World Health Organization (2022) Zika virus. <https://www.who.int/news-room/fact-sheets/detail/zika-virus>. Accessed 14 Jun 2022
- World Health Organization (2022) Coronavirus Disease. https://www.who.int/health-topics/coronavirus#tab=tab_1. Accessed 14 Jun 2022
- World Health Organization (2020) WHO coronavirus (Covid19): dashboard. <https://covid19.who.int/region/sear/country/in>. Accessed 14 Jun 2022
- Tamuzi JL, Ayele BT, Shumba CS et al (2020) Implications of COVID-19 in high burden countries for HIV/TB: a systematic review of evidence. *BMC Infect Dis* 20:1–18. <https://doi.org/10.1186/s12879-020-05450-4>
- World Health Organization (2021) Global tuberculosis report
- Tolossa T, Tsegaye R, Shiferaw S et al (2021) Survival from a triple co-infection of COVID-19, HIV, and tuberculosis: a case report. *Int Med Case Rep J* 14:611–615. <https://doi.org/10.2147/IMCRJ.S326383>
- Ortiz-Martínez Y, Mogollón-Vargas JM, López-Rodríguez M, Rodríguez-Morales AJ (2021) A fatal case of triple coinfection: COVID-19, HIV and tuberculosis. *Travel Med Infect Dis* 43:102129. <https://doi.org/10.1016/j.tmaid.2021.102129>
- Rivas N, Espinoza M, Loban A et al (2020) Case report: COVID-19 recovery from triple infection with mycobacterium tuberculosis, HIV, and SARS-CoV-2. *Am J Trop Med Hyg* 103:1597–1599. <https://doi.org/10.4269/ajtmh.20-0756>
- Farias LABG, Moreira ALG, Corrêa EA et al (2020) Case report: coronavirus disease and pulmonary tuberculosis in patients with human immunodeficiency virus: report of two cases. *Am J Trop Med Hyg* 103:1593–1596. <https://doi.org/10.4269/ajtmh.20-0737>
- Sarkar S, Khanna P, Singh AK (2021) Impact of COVID-19 in patients with concurrent co-infections: a systematic review and meta-analyses. *J Med Virol* 93:2385–2395. <https://doi.org/10.1002/jmv.26740>
- Zhu F, Cao Y, Xu S, Zhou M (2020) Reply to comments on ‘Co-infection of SARS-CoV-2 and HIV in a patient in Wuhan City, China.’ *J Med Virol* 92:1417–1418. <https://doi.org/10.1002/jmv.25838>
- Kumar R, Bhattacharya B, Meena V et al (2020) COVID-19 and TB co-infection-‘Finishing touch’ in perfect recipe to ‘severity’ or ‘death.’ *J Infect* 81:e39–e40
- Geldmacher C, Zumla A, Hoelscher M (2012) Interaction between HIV and Mycobacterium tuberculosis: HIV-1-induced CD4 T-cell depletion and the development of active tuberculosis. *Curr Opin HIV AIDS* 7:268–275. <https://doi.org/10.1097/COH.0b013e3283524e32>
- Hogan AB, Jewell BL, Sherrard-Smith E et al (2020) Potential impact of the COVID-19 pandemic on HIV, tuberculosis, and malaria in low-income and middle-income countries: a modelling study. *Lancet Glob Heal* 8:e1132–e1141. [https://doi.org/10.1016/S2214-109X\(20\)30288-6](https://doi.org/10.1016/S2214-109X(20)30288-6)
- Shyam M, Shilkar D, Verma H et al (2021) The mycobactin biosynthesis pathway: a prospective therapeutic target in the battle

- against tuberculosis. *J Med Chem* 64:71–100. <https://doi.org/10.1021/acs.jmedchem.0c01176>
41. Schrödinger Release 2022–1 (2021) Desmond molecular dynamics system, D. E. Shaw Research, New York, NY, 2021. Maestro-Desmond Interoperability Tools, Schrödinger, New York, NY
42. BIOVIA Dassault Systèmes (2021) Discovery Studio Visualizer. San Diego, CA, USA
43. Burley SK, Berman HM, Bhikadiya C et al (2019) RCSB Protein Data Bank: biological macromolecular structures enabling research and education in fundamental biology, biomedicine, biotechnology and energy. *Nucleic Acids Res* 47:D464–D474. <https://doi.org/10.1093/nar/gky1004>
44. Varadi M, Anyango S, Deshpande M et al (2022) AlphaFold Protein Structure Database: massively expanding the structural coverage of protein-sequence space with high-accuracy models. *Nucleic Acids Res* 50:D439–D444. <https://doi.org/10.1093/nar/gkab1061>
45. Hopkins AL, Ren J, Esnouf RM et al (1996) Complexes of HIV-1 reverse transcriptase with inhibitors of the HEPT series reveal conformational changes relevant to the design of potent non-nucleoside inhibitors. *J Med Chem* 39:1589–1600. <https://doi.org/10.1021/jm960056x>
46. Yin W, Mao C, Luan X et al (2020) Structural basis for inhibition of the RNA-dependent RNA polymerase from SARS-CoV-2 by remdesivir. *Science* 368(80):1499–1504. <https://doi.org/10.1126/science.abc1560>
47. Pettersen EF, Goddard TD, Huang CC et al (2004) UCSF chimera - a visualization system for exploratory research and analysis. *J Comput Chem* 25:1605–1612. <https://doi.org/10.1002/jcc.20084>
48. Rizvi SMD, Shakil S, Haneef M (2013) A simple click by click protocol to perform docking: Autodock 4.2 made easy for non-bioinformaticians. *EXCLI J* 12:830–857
49. Krieger E, Joo K, Lee J et al (2009) Improving physical realism, stereochemistry, and side-chain accuracy in homology modeling: Four approaches that performed well in CASP8. *Proteins Struct Funct Bioinforma* 77:114–122. <https://doi.org/10.1002/prot.22570>
50. Warren GL, Andrews CW, Capelli AM et al (2006) A critical assessment of docking programs and scoring functions. *J Med Chem* 49:5912–5931. <https://doi.org/10.1021/jm050362n>
51. Mujwar S, Kumar V (2020) Computational drug repurposing approach to identify potential fatty acid-binding protein-4 inhibitors to develop novel antiobesity therapy. *Assay Drug Dev Technol* 18:318–327. <https://doi.org/10.1089/adt.2020.976>
52. Jain R, Mujwar S (2020) Repurposing metocurine as main protease inhibitor to develop novel antiviral therapy for COVID-19. *Struct Chem* 31:2487–2499. <https://doi.org/10.1007/s11224-020-01605-w>
53. Mujwar S, Deshmukh R, Harwansh RK et al (2019) Drug repurposing approach for developing novel therapy against mupirocin-resistant *Staphylococcus aureus*. *Assay Drug Dev Technol* 17:298–309. <https://doi.org/10.1089/adt.2019.944>
54. Steffen C, Thomas K, Huniar U et al (2010) AutoDock4 and AutoDockTools4: automated docking with selective receptor flexibility. *J Comput Chem* 31:2967–2970
55. Morris GM, Goodsell DS, Halliday RS et al (1998) Automated docking using a Lamarckian genetic algorithm and an empirical binding free energy function. *J Comput Chem* 19:1639–1662. [https://doi.org/10.1002/\(SICI\)1096-987X\(19981115\)19:14%3c1639::AID-JCC10%3e3.0.CO;2-B](https://doi.org/10.1002/(SICI)1096-987X(19981115)19:14%3c1639::AID-JCC10%3e3.0.CO;2-B)
56. Mark P, Nilsson L (2001) Structure and dynamics of the TIP3P, SPC, and SPC/E water models at 298 K. *J Phys Chem A* 105:9954–9960. <https://doi.org/10.1021/jp003020w>
57. Jorgensen WL, Maxwell DS, Tirado-Rives J (1996) Development and testing of the OPLS all-atom force field on conformational energetics and properties of organic liquids. *J Am Chem Soc* 118:11225–11236. <https://doi.org/10.1021/ja9621760>
58. Gibson DA, Carter EA (1993) Time-reversible multiple time scale ab initio molecular dynamics. *J Phys Chem* 97:13429–13434. <https://doi.org/10.1021/j100153a002>
59. Cheng A, Merz KM (1996) Application of the Nosé-Hoover chain algorithm to the study of protein dynamics. *J Phys Chem* 100:1927–1937. <https://doi.org/10.1021/jp951968y>
60. Kalibaeva G, Ferrario M, Ciccotti G (2003) Constant pressure-constant temperature molecular dynamics: a correct constrained NPT ensemble using the molecular virial. *Mol Phys* 101:765–778. <https://doi.org/10.1080/0026897021000044025>
61. Kumar BK, Faheem SKVGC et al (2022) Pharmacophore based virtual screening, molecular docking, molecular dynamics and MM-GBSA approach for identification of prospective SARS-CoV-2 inhibitor from natural product databases. *J Biomol Struct Dyn* 40:1363–1386. <https://doi.org/10.1080/07391102.2020.1824814>
62. Jacobson MP, Pincus DL, Rapp CS et al (2004) A hierarchical approach to all-atom protein loop prediction. *Proteins Struct Funct Genet* 55:351–367. <https://doi.org/10.1002/prot.10613>
63. Selick HE, Beresford AP, Tarbit MH (2002) The emerging importance of predictive ADME simulation in drug discovery. *Drug Discov Today* 7:109–116. [https://doi.org/10.1016/S1359-6446\(01\)02100-6](https://doi.org/10.1016/S1359-6446(01)02100-6)
64. Daina A, Michielin O, Zoete V (2017) SwissADME: a free web tool to evaluate pharmacokinetics, drug-likeness and medicinal chemistry friendliness of small molecules. *Sci Rep* 7:1–13. <https://doi.org/10.1038/srep42717>
65. Pires DEV, Blundell TL, Ascher DB (2015) pkCSM: predicting small-molecule pharmacokinetic and toxicity properties using graph-based signatures. *J Med Chem* 58:4066–4072. <https://doi.org/10.1021/acs.jmedchem.5b00104>
66. Bylén F, Menéndez CA, Perez-Lemus GR et al (2021) Modeling the binding mechanism of remdesivir, favilavir, and ribavirin to SARS-CoV-2 RNA-dependent RNA polymerase. *ACS Cent Sci* 7:164–174. <https://doi.org/10.1021/acscentsci.0c01242>
67. Jockusch S, Tao C, Li X et al (2020) A library of nucleotide analogues terminate RNA synthesis catalyzed by polymerases of coronaviruses that cause SARS and COVID-19. *Antiviral Res* 180:104857. <https://doi.org/10.1016/j.antiviral.2020.104857>
68. Ju J, Li X, Kumar S et al (2020) Nucleotide analogues as inhibitors of SARS-CoV polymerase. *Pharmacol Res Perspect* 8:4690–4697. <https://doi.org/10.1002/prp2.674>
69. Baby K, Maity S, Mehta CH et al (2020) Targeting SARS-CoV-2 RNA-dependent RNA polymerase: an *in silico* drug repurposing for COVID-19. *F1000Research* 9. <https://doi.org/10.12688/f1000research.26359.1>
70. Liu X, Shi D, Zhou S et al (2018) Molecular dynamics simulations and novel drug discovery. *Expert Opin Drug Discov* 13:23–37. <https://doi.org/10.1080/17460441.2018.1403419>
71. Kennedy WP, Momand JR, Yin YW (2007) Mechanism for de novo RNA synthesis and initiating nucleotide specificity by T7 RNA polymerase. *J Mol Biol* 370:256–268. <https://doi.org/10.1016/j.jmb.2007.03.041>
72. Bose-Basu B, DeRose EF, Kirby TW et al (2004) Dynamic characterization of a DNA repair enzyme: NMR studies of [methyl-13C]methionine-labeled DNA polymerase β . *Biochemistry* 43:8911–8922. <https://doi.org/10.1021/bi049641n>
73. Shyam M, Shilkar D, Rakshit G, Jayaprakash V (2022) Approaches for targeting the mycobactin biosynthesis pathway for novel anti-tubercular drug discovery: where we stand. *Expert Opin Drug Discov* 1–17. <https://doi.org/10.1080/17460441.2022.2077328>